

TRIUMF Spring Work Report
SFU Co-op Department
Trim Coil Project
Applied Physics Major

Benjamin Sheldan

April 28, 2017

Contents

1	Introduction to TRINAT	3
2	Magnetic Fields from Basic Geometries	3
3	Circular vs. Square Coils and the Helmholtz Condition	5
3.1	The Helmholtz Condition	5
3.2	Circular vs. Square Coil Geometries	6
3.3	Near Helmholtz Arrangement	7
3.4	Experimental Data	8
3.5	Transverse Field Considerations	10
3.6	Field with Current Mu Metal Setup Added	12
4	Eddy Current Considerations	14
4.1	Eddy Currents - Theoretical Description	14
4.2	First Experimental Findings	15
4.3	Circuit Analysis	16
5	Waveform Design and Tests	19
5.1	Audio Amplifier	19
5.2	Easy-Wave Installation and Use	21
5.3	Kepeco Bipolar Supply	22
6	Photomultiplier Tube (PMT) Shielding	24
7	Shake-off Electron Detector	28
8	Programming Power Supplies	30
8.1	Terminal Emulators	30
8.2	Serial Command Basics	31
8.3	Serial Commands Using C++	32
9	Running the DC Trap on Stable Species	33
9.1	Stable Species Preliminary Trap Analysis	34
10	Acknowledgements	36
11	References	36
12	Appendices	37
12.1	Appendix 1: Physical Concepts	37

1 Introduction to TRINAT

In this report I will cover the basics of what physics Triumf’s Neutral Atom Trap (TRINAT) studies, my goals as an undergrad research assistant, and the results of my work this term. I will use this introduction to give a broad overview of the physics required to understand the TRINAT research, explain the experimental apparatus, and outline the following sections I have divided my report into. Terms outlined in bold are physical concepts which may not be familiar to all readers, and you may consult Appendix 1 for a library of useful definitions I have provided. TRINAT studies the effects of the **weak interaction** by observing **beta decay** in unstable species of atoms, such as potassium 37 in the process,



where a potassium atom has undergone beta plus decay producing a recoiling daughter nucleus, argon 37 (a proton has been turned into a neutron), a beta particle, in this case a positron in order to conserve the electric charge, and a neutrino. By trapping the short lived species (potassium 37 has a half-life of around 1.24s [1]) the energy and momenta of the parent nucleus are well known. The trap is turned on and off to allow for **spin polarization** of the atoms between trapping periods. The trapping period occurs for a duration of 1ms , and the same for the optical pumping period where the atoms are polarized. The timing is set to reduce the number of atoms that escape the trap from collisions during the optical pumping. The actual trap itself inside the main vacuum chamber is a Magneto-Optical Trap (MOT) and consists of anti-Helmholtz coils which are explained in detail in a following section creating a **quadrupole field** and a laser trap that works on the principles of **Doppler cooling**. The potassium 37 atoms are confined to, roughly, a cubic millimeter volume. Since the atoms are highly polarized, the direction of emission of the recoil nucleus and beta particle, due to conservation of angular momentum (which spin is a component of), can be calculated and using detectors the momenta of the recoil nucleus and beta particle are directly observed. The momentum of the **neutrino** is deduced by the conservation of momentum law. Comparing spin polarized observables for these atoms undergoing beta decay against predicted Standard Model (SM) values, TRINAT is able to search for and constrain physics beyond the SM.

My work this term has been focused on whether it would be viable to implement a set of trim coils on the main vacuum/trap chamber, assist in the assembly and setup for calibration of an upgraded shake-off electron microchannelplate (MCP) detector, remote control programming of replacement power supplies, as well as integrating code for an automated sweep with the power supplies to optimize the trap location based on the field produced during the sweep of current output from the supplies. I will begin with calculations of the magnetic field produced by the trim coils and their comparison with the experimental data I acquired from a mock test setup. As mentioned previously, the trap is turned on and off with a 2ms periodicity which would be required for these trim coils as well. This took much longer than first expected as eddy currents induced by the changing magnetic field had much larger effects than first anticipated. In order to reduce these eddy current effects, I designed an optimized waveform to drive the current in the coils and I will discuss the various power supplies used including a “Russian Coil” driver, audio amplifier, and finally the Kepco Bipolar supply used to run the waveform. I will discuss how mu-metal shielding works and how it can be used to shield sensitive photomultiplier tube (PMT) detectors from external magnetic fields (ie, the ones generated by my large trim coils). I will discuss how the electron microchannel plate detector works and the basics of sending serial commands and programming them in C and C++ which I used to control the replacement Tenma DC power supplies. Lastly, I will end with an outline of how to locate the required files for running/modifying the code for the trap and Flea camera (written and upgraded by previous co-op students Claire Preston and Liam Lawrence) and the additions I made for controlling the power supplies.

2 Magnetic Fields from Basic Geometries

First, I will begin with some magnetic fields created from basic geometries of current flow, and by extension the methods used for more involved geometries. These will be important to refer to later as a check in limiting cases of formulas I derive for more complicated geometries. To simplify the math for all following cases, I assume that the thickness of the wire is negligible compared to the dimensions of the geometry I am considering, and later when I present my experimental data, this assumption is justified. For

a wire of infinite length Ampere's Law [2] can be used,

$$\oint \vec{B} \cdot d\vec{s} = \mu_0 I_{enc}, \quad (2)$$

where \vec{B} is the magnetic field at the point I wish to calculate, $d\vec{s}$ is the infinitesimal line segment of the Amperian loop, μ_0 is the permeability of free space, and I_{enc} is the enclosed current. For an infinite wire, there is cylindrical symmetry and drawing an Amperian loop of a circle at a radius s from the wire, \vec{B} can be pulled out of the integral as it is constant, the enclosed current in the wire is simply I , and the path is an integral along the circumference of a circle,

$$B \int_0^{2\pi} s d\theta = \mu_0 I, \quad (3)$$

which is trivial to solve,

$$\vec{B} = \frac{\mu_0 I}{2\pi s} \hat{\phi}, \quad (4)$$

where $\hat{\phi}$ is the azimuthal angle by using the familiar right-hand rule. Although this is an extremely simple case, it will prove useful to test limiting cases in further derivations.

For further geometries where Amperian symmetry is absent it will be necessary to use the Biot-Savart Law [2],

$$d\vec{B} = \frac{\mu_0 I}{4\pi} \frac{d\vec{l}' \times (\vec{r} - \vec{r}')}{|\vec{r} - \vec{r}'|^3}, \quad (5)$$

where $d\vec{l}'$ is the infinitesimal wire segment, \vec{r} is the vector to the point at which the magnetic field is being calculated, and \vec{r}' is the vector to the wire segment being integrated over. Using the Biot-Savart Law, the equation for a finite wire segment was found to be,

$$\vec{B} = \frac{\mu_0 I}{4\pi s} (\cos\theta_2 + \cos\theta_1) \hat{\phi}, \quad (6)$$

where s is the radial distance from the wire to the magnetic field point and the angle θ_i is the angle between the line drawn from one end of the wire to the point at which the magnetic field is calculated at and the wire.

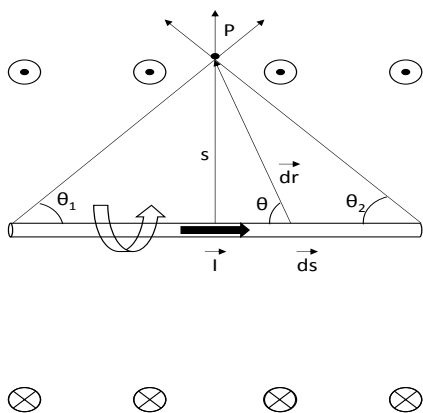


Figure 1: Biot-Savart Law setup for a finite wire of length L , where the magnetic field is calculated at a radial distance from the wire. This setup is also used for calculating the field from a square loop by integrating over four finite wires.

Taking the limiting case of an infinite wire, where both angles approach 0, ($\cos(0) = 1$) equation 4, describing the field from an infinite wire is recovered. Now that I have given an idea of how to go about

using the Biot-Savart Law to calculate the resulting magnetic field from a given geometry of wire, I will simply present additional formula I have derived in my notes without going into exhausting mathematical detail. The circular loop is obtained by integrating around a wire at a given radius R , and the square loop by adding the results of multiple finite wires. Below are the expressions for the magnetic field along the axis of such current loops. Both the circular and square loop are sitting in the xy -plane with their axis oriented along the \hat{z} direction.

Circular Loop:

$$\vec{B}_{circ,z} = \frac{\mu_0 I}{2} \frac{R^2}{(z^2 + R^2)^{3/2}} \hat{z} \quad (7)$$

Where R is the radius of the coils.

Square Loop:

$$\vec{B}_{square,z} = \frac{4\mu_0 I}{\pi} \frac{L^2}{(4z^2 + 2L^2)^{1/2}(4z^2 + L^2)} \hat{z} \quad (8)$$

where L is the length of one side of the square coil. My first analysis, which will be the focus of the following section, will be to consider whether there is a preference over circular or square coil geometry as well as considerations about the Helmholtz condition.

3 Circular vs. Square Coils and the Helmholtz Condition

3.1 The Helmholtz Condition

There are various reasons to desire a uniform magnetic field in an experimental setup such as canceling Earth's magnetic field. If possible, a solenoid is often used which creates an extremely uniform field along its axis [4],

$$\vec{B}_z = \frac{\mu_0 N I}{2L} \left[\frac{z - \frac{L}{2}}{((z - L/2)^2 + R^2)^{1/2}} - \frac{z + \frac{L}{2}}{((z + L/2)^2 + R^2)^{1/2}} \right] \hat{z}, \quad (9)$$

where N is the number of turns, L is the length of the solenoid, R is the radius, and the equation reduces to $\vec{B} \approx \mu_0 \frac{NI}{L} \hat{z}$ for the length of the solenoid when $L \gg R$. However, in many experimental conditions a solenoid cannot be implemented because of other equipment. This is the case with the TRINAT setup as we have additional coils outside the chamber for canceling Earth's field, as well as PMTs for photon detection, cameras, an entry port for the atoms delivered via a push-beam, and various other reasons. The other approach for producing a small region of uniform magnetic field is the Helmholtz setup. Helmholtz coils are a well known design where two loops of coil, they can be circular, square or rectangular, are coaxially separated by a small distance and the field along the coil axis near the center is relatively uniform. There are several steps to showing this uniformity. For any of the three geometries (circular, square or rectangular) it is easy to show that after defining the origin of the coordinate system to be at the midpoint between coils, if coils are placed in the plane perpendicular to the \hat{z} direction above and below the axis at locations $z = \frac{d}{2}$ and $z = -\frac{d}{2}$ such that the coils are separated a total distance of d , the field is already uniform at the center point due to symmetry.

For the circular coil configuration, where the coils are separated by a distance d , placed symmetrically above and below the xy -plane, the overall expression for the magnetic field, using equation 7, will be,

$$\vec{B}_z = \frac{R^2 \mu_0 I}{2} \left[\frac{1}{((z - d/2)^2 + R^2)^{3/2}} + \frac{1}{((z + d/2)^2 + R^2)^{3/2}} \right] \hat{z}, \quad (10)$$

and it is easy to show that $\frac{dB}{dz}|_{z=0} = 0$ due to the symmetry of the placement of the coils. For constructing a more uniform magnetic field, the Helmholtz condition is achieved by setting $d = R$, and it can be shown

that both $\frac{d^2 B}{dz^2}|_{z=0}$ and $\frac{d^3 B}{dz^3}|_{z=0}$ vanish at the center point ($z = 0$) as well. The same follows for square coils,

$$\vec{B}_z = \frac{4\mu_0 I L^2}{\pi} \left[\frac{1}{(4(z-d/2)^2 + 2L^2)^{1/2}(4(z-d/2)^2 + L^2)} + \frac{1}{(4(z+d/2)^2 + 2L^2)^{1/2}(4(z+d/2)^2 + L^2)} \right] \hat{z}, \quad (11)$$

where I calculated the Helmholtz separation distance such that the second and third derivatives of the field vanish at $z = 0$ to be $d = 0.54451L$ where L is the length of one side of the square loop. And again, I constructed the same scenario for a rectangular loop of coils,

$$\vec{B}_z = \frac{2\mu_0 I l_1 l_2}{\pi} \left(\frac{1}{(4(z-d/2)^2 + l_1^2 + l_2^2)^{1/2}} \left[\frac{1}{(4(z-d/2)^2 + l_1^2)} + \frac{1}{(4(z-d/2)^2 + l_2^2)} \right] + \frac{1}{(4(z+d/2)^2 + l_1^2 + l_2^2)^{1/2}} \left[\frac{1}{(4(z+d/2)^2 + l_1^2)} + \frac{1}{(4(z+d/2)^2 + l_2^2)} \right] \right) \hat{z}, \quad (12)$$

where I found the Helmholtz separation to be $d \approx 0.5445L_{avg}$ where L_{avg} is an average of the two side lengths of the rectangle, $L_{avg} = \frac{l_1 + l_2}{2}$. As a check, in the limit that $l_1 = l_2 = L_{avg} \equiv L$ both equation 11, the field expression for square coils, and $d = 0.5445L$, the Helmholtz condition for square coils are recovered.

3.2 Circular vs. Square Coil Geometries

After setting the Helmholtz conditions, $d = R$ and $d = 0.5445L$, I used WaveMetrics software [3], and formulas 10 and 11 to test whether circular versus square coils produced noticeable field variations along the field axis. I also compared the region of uniformity as the size of the coils increased.

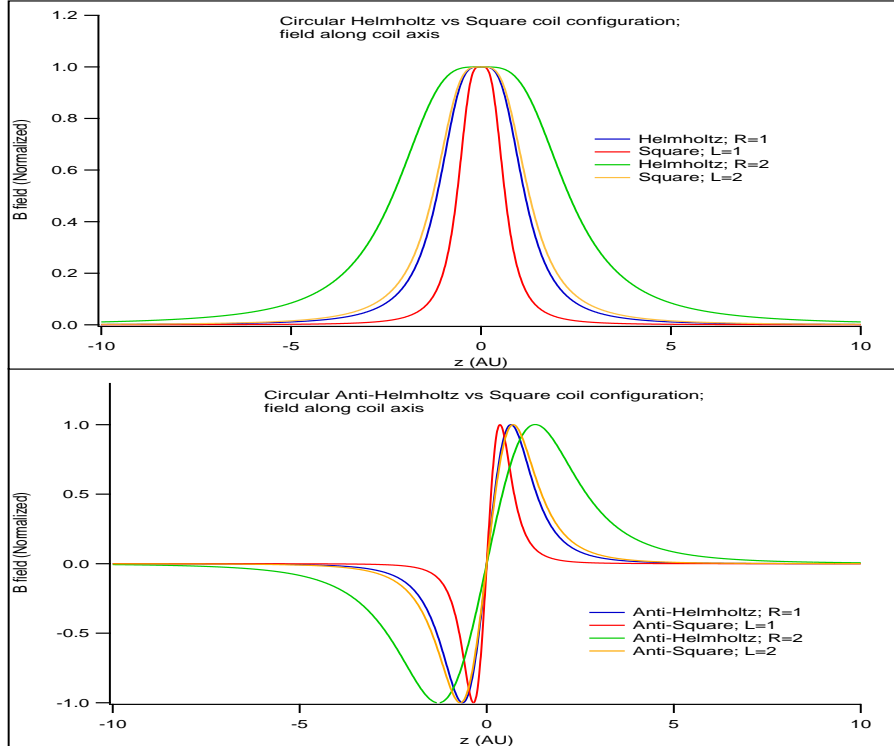


Figure 2: Theoretical plots of the magnetic fields, generated using WaveMetrics, produced along the coil axis for square and circular geometries that satisfy the Helmholtz condition.

Rectangular plots are not shown as they did not show any difference from the square coil setup when $L_{avg} \approx L$. There were noticeable divergences in the field behavior when $l_1 \gg l_2$ or vice versa, but for my experimental setup $l_1 = 1.33l_2$ and the qualitative behavior can be interpreted from simply plotting the

field produced by square coils. The simulated magnetic field plots have several key features. For square and circular coils when the side length of the square loop is equal to the diameter of the circular coils, $L = 2R \equiv D$, the fields along the coil axis show the same magnitude and general properties, including a region of identical uniformity around the origin, $z = 0$. The only difference is that the square field decays slightly slower as $z \Rightarrow \pm \infty$. The other main qualitative feature is that the larger the coils, the larger the region of uniformity near the center. However, the problem to keep in mind here is the same as with implementing magnetic fields from a solenoid, and whether coils of a certain size will fit in the experimental apparatus must be considered, but the general principle of either using solenoidal geometries, or large Helmholtz coils where possible will give the best results for a region of uniform magnetic field. Also, from the consideration of the magnetic field produced along the coil axis, there is no preference to circular, square, or rectangular coils and any of these geometries will work.

I have also included plots of the anti-Helmholtz arrangement for completeness. Anti-Helmholtz coils are identical to the Helmholtz setup previously described except that current is flowing in opposite directions in the coils rather than in the same direction. This produces a point of zero magnetic field in the center and field of opposite sign across the $z = 0$ plane. This setup is used in the MOT by TRINAT. If atoms move away from the center, for small displacements the magnetic field changes linearly in magnitude and induces a Zeeman shift in the energy level of the atoms. This means that as an atom moves further from the center of the trap the transition level in the atom is shifted closer and closer to the frequency at which the laser is tuned to (see Appendix 1 on why the laser is slightly detuned) and it is more probable that the atom will absorb a photon and by conservation of momentum, will receive an impulse back towards the trap.

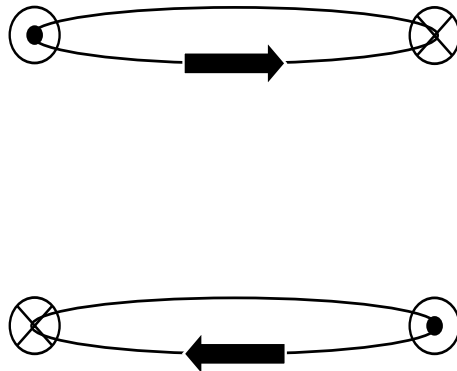


Figure 3: Current flow in a pair of anti-Helmholtz coils which create a quadrupole field.

In Fig. 3, the cross depicts current flowing into the page, and the dot represents current flowing out of the page. By having the coils anti-aligned and looking at the resulting magnetic field lines, [5] displays a nice contour plot of the magnetic field, the resulting field has the same general qualitative behavior as if we were looking at the electric field created by two $+q$ and two $-q$ charges.

3.3 Near Helmholtz Arrangement

The next point to consider was the size of the chamber itself and whether it is possible to implement Helmholtz coils and, if not, what is the effect on the magnetic field and does it still work for our purposes. After measuring the size of the chamber and looking at what space was viable, I determined that the smallest separation of the coils possible was 46cm (18"). Also due to the cylindrical nature of the chamber, rectangular coils would be the easiest to implement. This meant that to satisfy the Helmholtz condition, I would need an average side length of 84.5cm. With entry ports, optical equipment, and detectors, there is not adequate space around the main chamber. However, the cloud of trapped atoms is confined to a small volume, about a cubic millimeter, so a relatively small region of uniformity would still suffice for our purpose. Using the expression for circular coils (the results hold for square and circular coils as well), 9, I plotted simulated

data for the resulting magnetic field as the separation is increased further and further outside the Helmholtz condition. There are several important points to make here. First, even for large separations of the coils, due to the symmetry of the expressions, the point along the coil axis at $z = 0$ will always have a zero derivative. The further away from Helmholtz separation, however, the increasing slope indicates that the magnetic field will change more rapidly as you move further from $z = 0$. Also, from mathematical analysis, when the Helmholtz condition is not met, $\frac{d^2B}{dz^2}|_{z=0}$ is also non-zero. After constructing rectangular coils and mounting them around a mock chamber to simulate the experimental trap chamber, I used a milligauss meter to verify the magnetic field along the coil axis to test how uniform the magnetic field was over a $10 \times 10 \times 5 \text{ cm}$ region around the origin. (I have taken the origin to be the exact center of the chamber). After reporting on these experimental findings, I will go on to consider the transverse magnetic fields, B_x and B_y , as well as comparing the field along the coil axis with and without the cylinders of mu-metal. The mu-metal cylinders were placed there to simulate the actual mu-metal shielding of the PMTs on the main trap chamber.

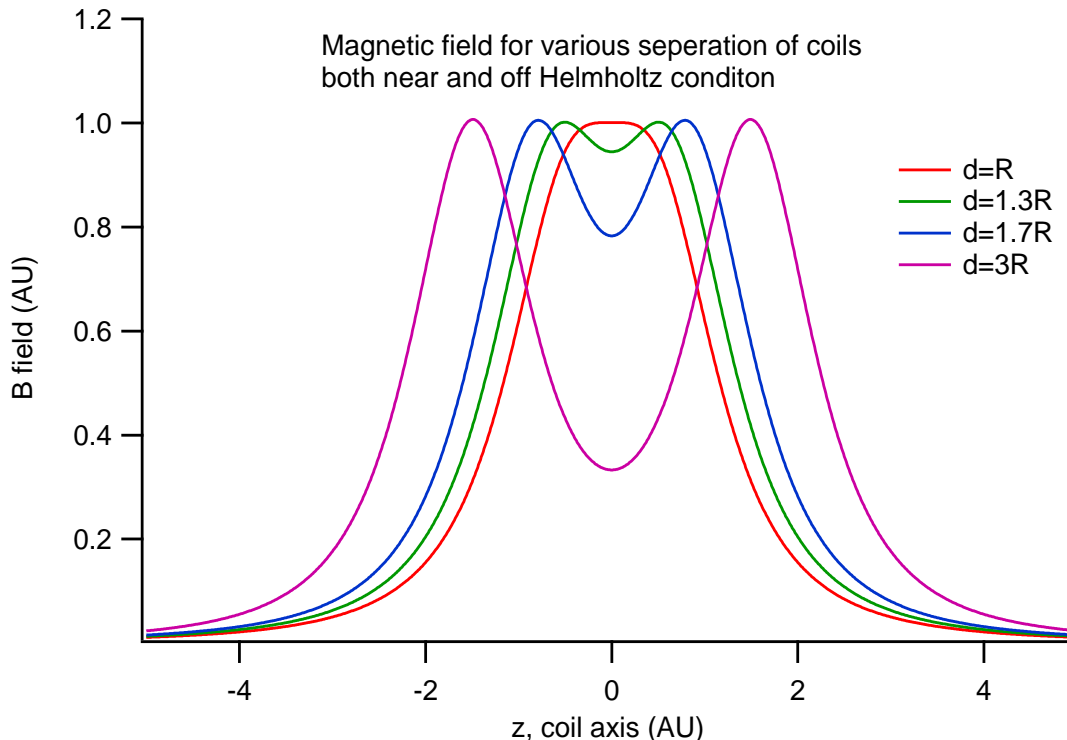


Figure 4: Simulated magnetic field data for circular coils placed at the required Helmholtz separation and at distances greater than the Helmholtz condition.

3.4 Experimental Data

As shown in Fig. 5, I constructed rectangular coils and placed them around a stainless steel cylinder to simulate the coils that would be added to the main experimental chamber setup. The chamber is 30.5 cm (12") in outer diameter, with a thickness of about 0.5 cm ($3/16$ "). Optical posts 7.6 cm (3") in length were fastened at the center of the chamber, midway along one of the coil sides, to fasten the coils in place, keeping them placed symmetrically around the chamber at a total separation distance of 45.7 cm (18"). The coils themselves were 45.7 cm (18") by 61 cm (24"). The coils were wound with 13 turns each and two DC power supplies were used to apply a current of 4.998 A to either coil. For the coils on the experimental chamber, our desired bias field is 2 G , which would require either more turns of wire or higher current DC power supplies as $|\vec{B}| \propto NI$ where N is the number of turns and I is the current.

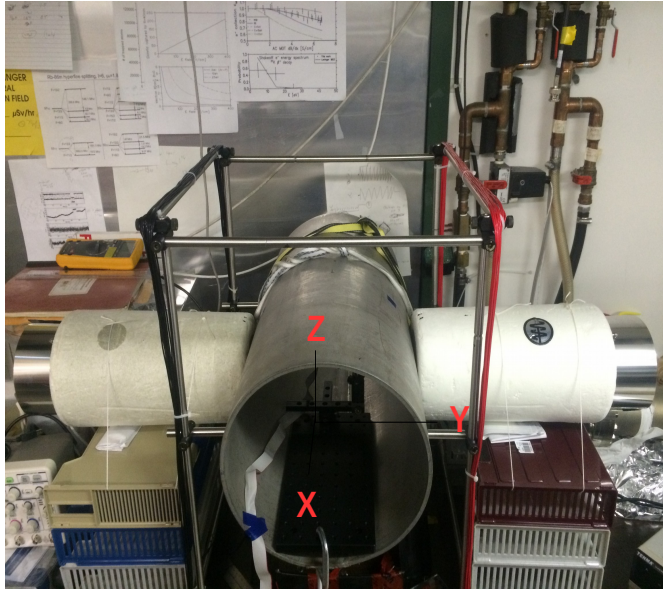


Figure 5: Stainless steel mock chamber to mimic the main trap chamber for taking experimental data. Axis are defined to match the labeled orientation of the milligauss meter used.

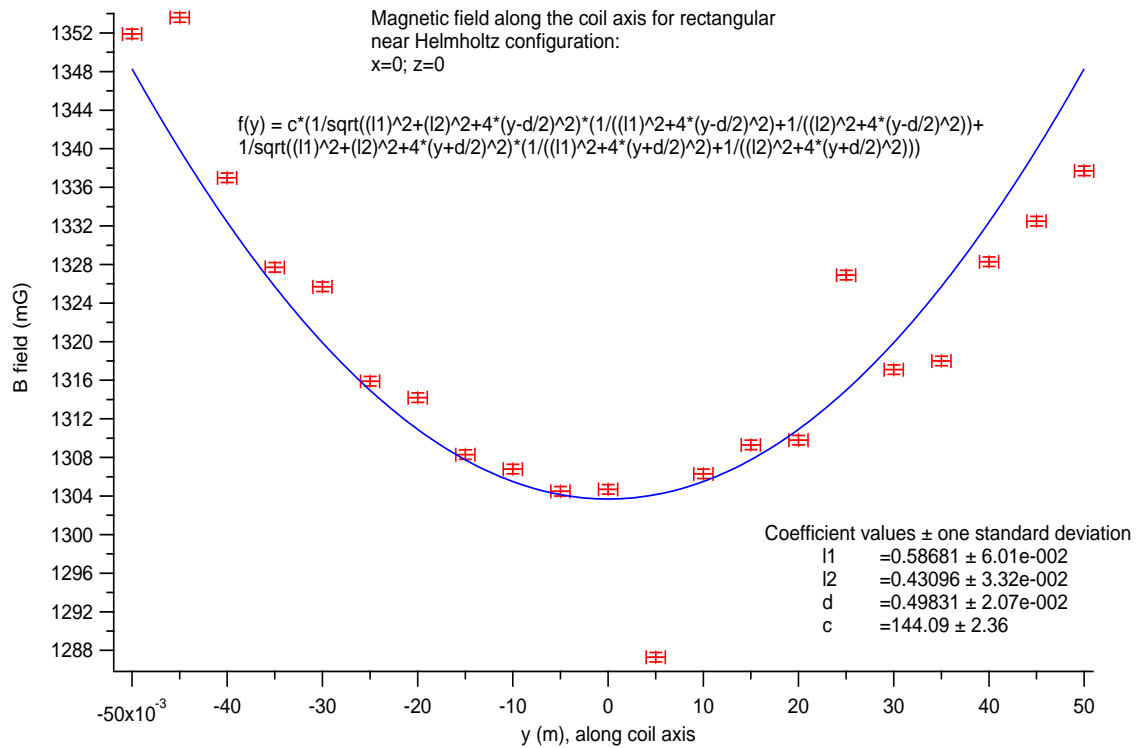


Figure 6: Experimental data obtained for the magnetic field along the coil axis.

The first experimental data sets were taken without mu-metal placed beside the chamber. The milligauss magnetic field probe was mounted on an aluminum optical post, on sliding optical trays and placed on an optical breadboard inside the chamber. Due to variations in the background fields around the room, two data points were taken for each location, with and without the coils turned on, and the difference between total field and background field is plotted above. Uncertainties in the field measurements were (over)estimated by using the size of fluctuations seen on the probe and uncertainties on the position measurements were inflated due to the fact that it was difficult to see and place a ruler inside the chamber. There are several things I will point out about this experimental data and the equipment used. Fluctuations of less than $2mG$ were seen when measuring both the total field with the coils on, and when measuring the background. This tells me that it is not the power supplies that are fluctuating in current (I had them set to current control mode), but rather either the magnetic fields in the room are varying or the milligauss meter has a small amount of drift. However, after adding the mu-metal to the system later the stray magnetic fields fluctuations were reduced leading me to conclude the background fields varied by small amounts on small times scales (seconds). While taking measurements one day, in the space of 15 minutes, the magnetic field probe drifted several hundred milligauss before returning to its normal state and this occurred several times that day. There were no issues like this on any other day I was taking data, but it is something to keep in mind when using this probe. Also, during a presentation that Dr. Behr attended, he let me know that another research group ran into the same scenario when using the same model of probe and it is possible there is a flaw in this specific model of magnetic field probe. For these reasons, I would be able to justify removing the point at $y = 5mm$ which is clearly anomalous.

Aside from that, in the region of $\pm 10mm$ from the center of the chamber, the field variations are, at most, $2mG$. Therefore, for our purposes of trapping atoms in a roughly $1mm^3$ cubic volume, the field is quite uniform. As the field strength linearly depends on the number of turns and current and does not change its characteristics, to increase from $1.3G$ to $2G$, the current or number of turns must increase by a factor of 1.5. Increasing the field by a factor of 1.5 changes the field variations from $2mG$ to $3mG$, an extremely small change, and still acceptable for our system. In summary, although these coils do not meet the Helmholtz condition, for a small region of $\pm 5mm$ millimeters at the center of the chamber, the field is relatively uniform and variations for a $2G$ bias field would be $2mG$ at maximum and the closer to the center of the chamber the smaller these variations would be. The next step was to consider the size of the transverse fields, B_x and B_z , for small displacements from the coil axis, where by symmetry, transverse fields are zero along the coils axis. This is easy to see that for every component of coil creating a transverse field, there is an identical segment from the other side of the coil to cancel that field contribution. (This is clearly true for each coil separately).

3.5 Transverse Field Considerations

In general, from reading literature on magnetic field simulations, aside from the classic 'textbooks' scenarios such as the field along a coil axis for a circular or square loop, solenoids, and other systems with a lot of symmetry present, analytic expressions for the total field, $\vec{B}(x, y, z)$, are complicated to write down. Although we have an explicit prescription for calculating the field from any geometry, equation 5, the Biot-Savart Law can be difficult to implement in practice. In order to simplify the calculations and derive an analytic expression, I will consider transverse fields in the xz -plane (where y is along the coil axis as shown in Fig. 5). For considering transverse fields in the xz -plane the vector from the origin to the point where I am calculating the field will be defined as $\vec{r} = x\hat{x} + z\hat{z}$. I will go into some explicit detail for the mathematical derivation of the expressions for the transverse fields such that the assumptions and limitations of these expressions are transparent. For a given wire segment, for example the wire parallel to x axis, placed at $z = L/2$, $y = -d/2$ will have a coordinate vector $\vec{r}' = L/2\hat{x} + y'\hat{y} - d/2\hat{z}$. I will integrate along $dx'\hat{x}$ and will need to evaluate the cross product, $d\vec{l}' \times (\vec{r} - \vec{r}')$ which, after substituting the vectors specified previously, is $dx'\hat{x} \times [(x - x')\hat{x} - d/2\hat{y} + (z - L/2)\hat{z}]$. After evaluating the cross product and setting up the integral form of the Biot-Savart Law I end up with,

$$\frac{-\mu_0 I}{4\pi} \left(\frac{d}{2} \hat{z} + \left(z - \frac{L}{2} \right) \hat{y} \right) \cdot \int_{-L/2}^{L/2} \frac{dx'}{\left((x - x')^2 + \frac{d^2}{4} + \left(z - \frac{L}{2} \right)^2 \right)^{3/2}}. \quad (13)$$

Evaluating the integral term,

$$\frac{8(x-x')}{(d^2 - (L-2z)^2)(4x^2 - 8xx' - d^2 + (L-2z)^2 + 4x'^2)^{1/2}} \Big|_{-L/2}^{L/2}, \quad (14)$$

and applying the bounds at $x' = -L/2$ and $x' = L/2$,

$$|\vec{B}_z| \propto \frac{8(x - \frac{L}{2})}{(d^2 - (L-2z)^2)(4x^2 - 4xL - d^2 + (L-2z)^2 + L^2)^{1/2}} - \frac{8(x + \frac{L}{2})}{(d^2 - (L-2z)^2)(4x^2 + 4xL - d^2 + (L-2z)^2 + L^2)^{1/2}}, \quad (15)$$

where the proportionality constant is given by $\frac{\mu_0 I d}{4\pi}$. As a check, by plugging $x = z = 0$ into the \hat{y} term in equation 15 I recover the expression for the azimuthal field from a finite wire (6), where $\cos(\theta)$ can be rewritten in terms of the length of the wire and the distance to the field point P. I can repeat this process for each of the eight wire segments that make up the two loops and sum the result.

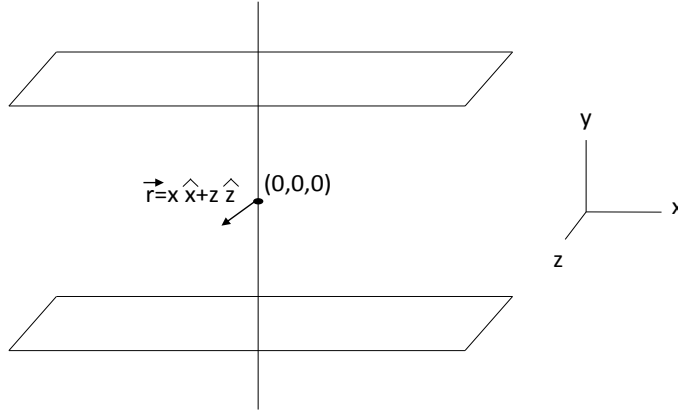


Figure 7: Diagram for the derivation of the transverse fields in the xz -plane from a pair of rectangular coils. L is defined to be the side length of the coils and d is their separation distance.

For the transverse fields from the square loops, as I wish to consider small Δx displacements from the origin (as the atom cloud is very small compared to the coil dimensions) the displacements will be small compared to the coil dimensions ($x, z \ll d, L$). I can disregard the x^2, z^2 terms in the denominator and Taylor expand with respect to x, z . The resulting equation,

$$|\vec{B}_z| = \frac{\mu_0 N I}{4\pi} d(1.75 + 9.56z + 44.24z^2)8L\Delta r, \quad (16)$$

for the transverse fields generated is greatly simplified. This expression predicts that for small displacements from the origin, the transverse magnetic fields will increase linearly. Next, I gathered experimental data to verify the expressions for transverse magnetic fields, verifying their magnitude. In the following figure, Fig. 8, I report on the experimental data obtained for the transverse fields in the \hat{x} direction for displacements along the coil axis, \hat{y} . For the $x = z = 0$ scenario, one would expect, and I have explicitly stated earlier, the transverse magnetic field should be zero. However, due to the size of the optical breadboard, mounts, and the magnetic field probe itself, the minimum z displacement I was able to achieve was $\sim 5mm$. However, I was able to verify my expressions, both the characteristics and magnitude of the transverse fields. The transverse fields increase linearly as the displacement from the origin increases, the rate of change of the transverse fields increases as displacement in the transverse direction increases. For displacements in the

xz -plane of less than a centimeter, I can plug in any value I wish, say $z = 5\text{mm}$ and $\Delta r = 1\text{cm}$, and I see that I expect transverse fields of $\leq 5\text{mG}$. The milligauss meter reported that it was accurate to a milligauss but due to fluctuations in background between taking a background and total field measurement, as well as not having a specifications for how large of a region to probe was averaging over (the probe housing was $1.5 \times 1.5 \times 3\text{cm}$, and I did not have a specification for how large the actual sensor was), field measurements near to $x = y = z = 0$ were hard to measure precisely. However, despite that, my experimental data shown in Fig. 8 show that my model predicts the size of the transverse fields accurately. By comparing slopes of the plots at various x values, I conclude that the rate of change of the transverse fields increases linearly with x . For a given displacement in one direction, the transverse fields increase linearly along the coil axis and go to 0 at $y = 0$. Also, for displacements of $\leq 1\text{cm}$, the transverse fields are, at most, around 5mG . Also, due to difficulty mounting the probe, the point $y = 0$ may not look to sit exactly at $B = 0$ and this is because the probe also has at least 5mm displacement in the \hat{z} direction as mentioned previously. Data obtained for the other transverse component follows the same characteristics so here I only display one of graphs.

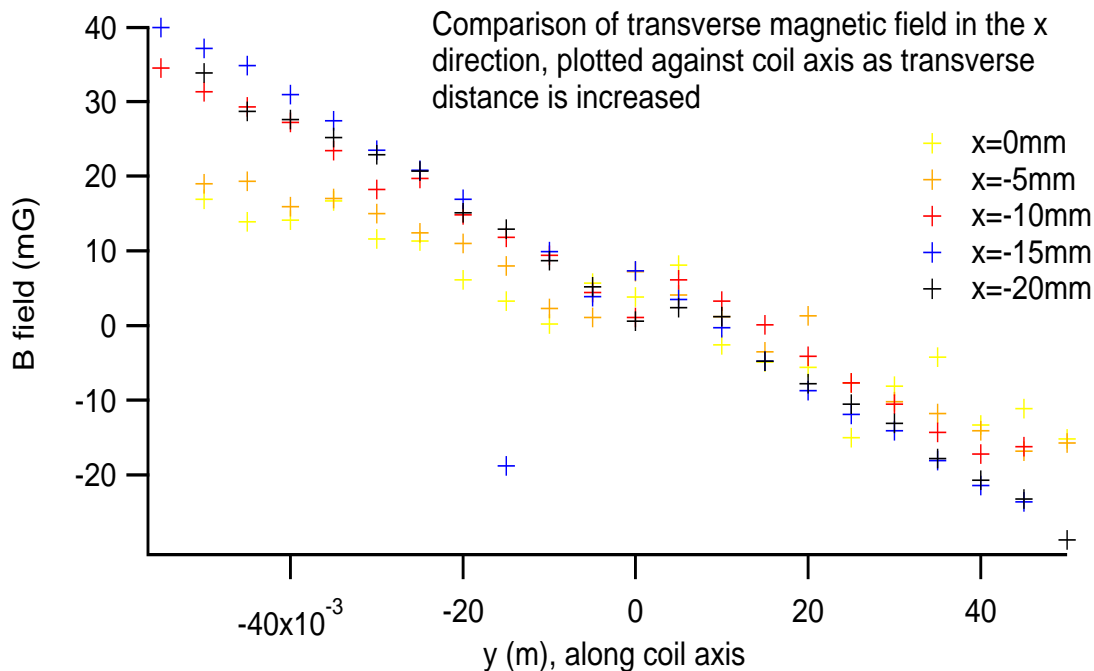


Figure 8: Experimental data obtained for the transverse magnetic fields along the coil axis at various displacements in the \hat{x} direction.

3.6 Field with Current Mu Metal Setup Added

In the current setup on the main experimental chamber, there are two mu-metal cylinders surrounding PMTs to shield them from the magnetic fields generated by the AC-MOT and Earth canceling near Helmholtz coils that are currently mounted horizontally around the chamber. The basic idea of magnetic shielding is this, the lowest order term that a magnetic field source will come from is a dipole (magnetic monopoles have been theorized but never experimentally verified) and field lines must always connect between the N-S poles (you can think of the field lines from a bar magnet). Since you cannot “stop” or “break” magnetic field lines and prevent them from completing their N-S path, magnetic shielding simply provides an alternate, desirable path for them to take and can be used in protecting sensitive equipment. Magnetic shielding material, such as mu-metal, acts like a magnetic field line conductor, drawing in the field and increasing the flux near the edge and within the material and in turn this decreases the flux of field lines inside the shield, attenuating the strength of the magnetic field.

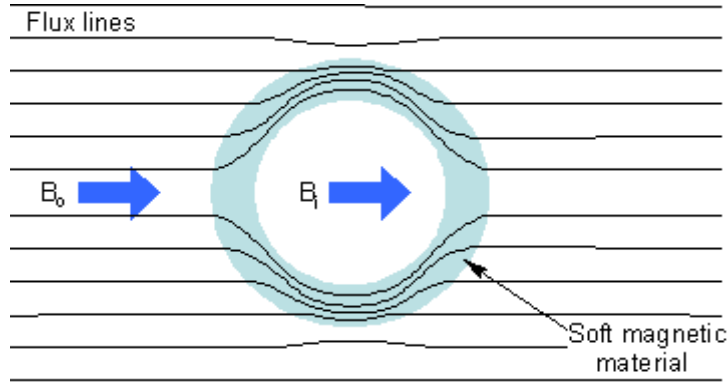


Figure 9: Visual reference for magnetic shielding [6].

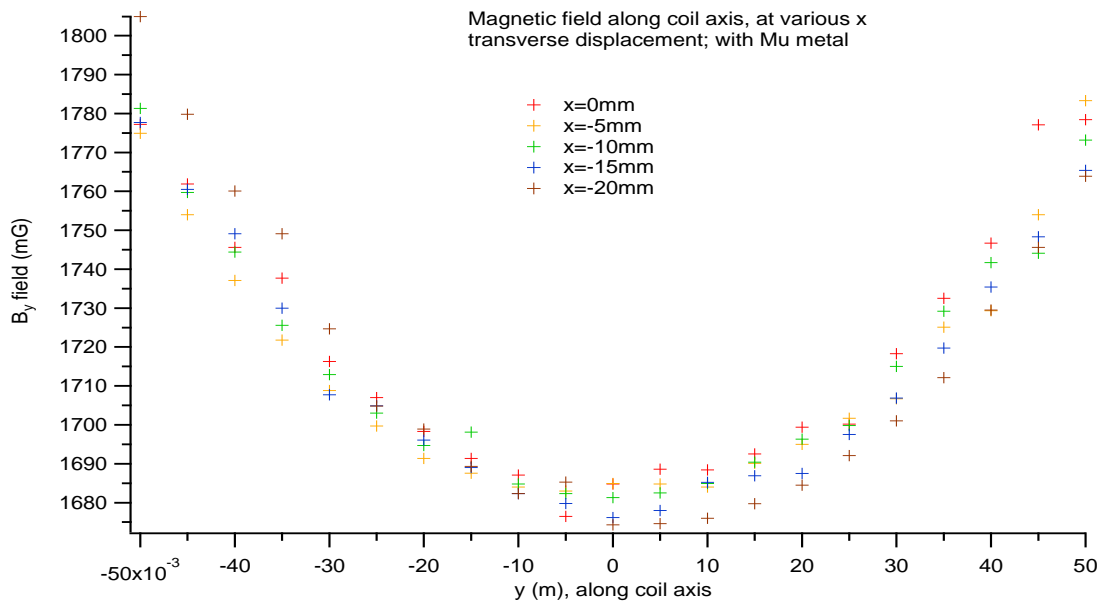


Figure 10: Experimental data obtained for the magnetic field along the coil axis, with mu-metal added to the system as shown in Fig. 5.

The experimental data obtained with mu-metal added to the system agree with intuition. Comparing Fig. 10 and 11 with 6 and 8, there are notably less fluctuations in the data. The mu-metal appears to help reduce small fluctuating background fields and noise. The field along the coil axis is relatively uniform over the same region previously discussed, the symmetry of the added mu-metal prevents non-uniformities from occurring. Also, due to the increase in flux the field strength increases by almost 400mG at the center of the chamber. This will need to be kept in mind when adjusting the current and number of turns for creating a 2G bias field on the experimental chamber. I will discuss more of the theory of mu-metal shielding and the effect on the magnetic field inside the mu cylinder in the section of PMT shielding later. For the transverse fields, in the region we are concerned with, $x, z \leq 1\text{cm}$, there is no change in the characteristics or magnitude. The linear dependence of the transverse fields on radial displacement and increase in slope with transverse displacement is conserved. However, at distance of greater than 5cm , it is clear that the transverse fields are also effected by the increase in flux and have increased in magnitude as well. After verifying the models I had developed for characterizing the DC magnetic field and determining that the magnetic field had the attributes we desired, it was time to consider the next step. During optical pumping and trapping, which are alternated every millisecond, this magnetic field would need to be turned on and off. In the following section I will discuss the physics associated with a time-varying magnetic field, the equipment used to drive

the current producing the magnetic field, and the number of experimental issues I faced while attempting to design a setup that would allow me to turn on and off the field in a relatively quick manner.

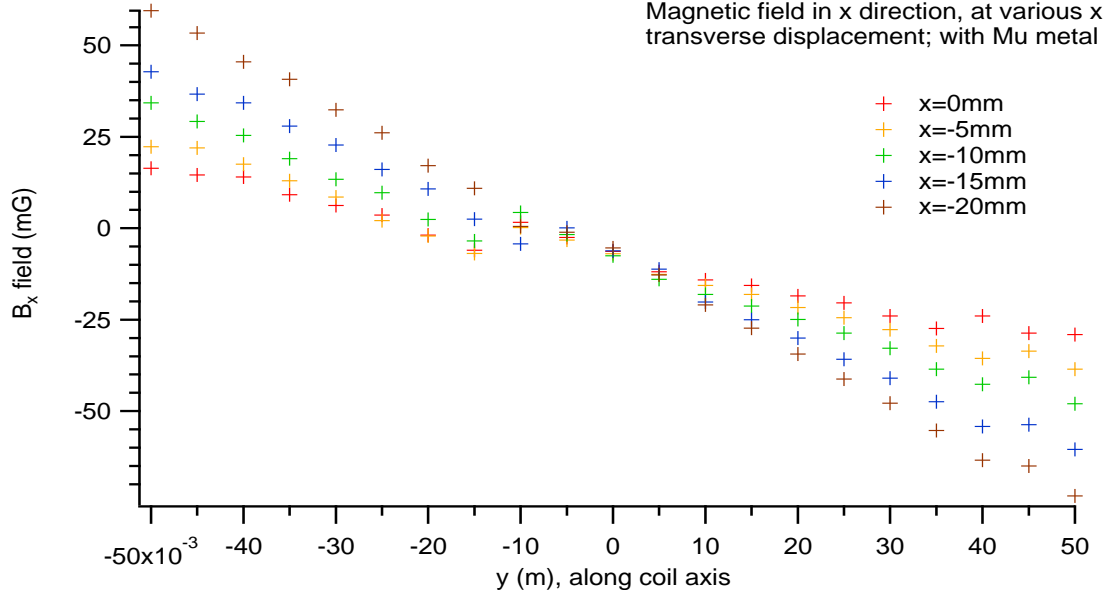


Figure 11: Experimental data obtained for the transverse magnetic fields, with mu-metal added to the system.

4 Eddy Current Considerations

4.1 Eddy Currents - Theoretical Description

For my experimental setup (and on the main trap chamber) for studying the characteristics of the DC magnetic field, it was sufficient that all nearby materials (stainless steel chamber and aluminum optical mounts), other than the mu-metal of course, be non-magnetic such that they do not interfere with the field desired at the trap location. However, when analyzing the effects of turning the field on and off, I needed to consider on of Maxwell's equations [2],

$$\vec{\nabla} \times \vec{E} = -\frac{\partial \vec{B}}{\partial t}, \quad (17)$$

that relates the time derivative of a magnetic field to the curl of an electric field. In other words, a magnetic field that varies with time will induce an electric field. Using the properties of vector calculus, I can rewrite the differential form of Maxwell's equation as,

$$\oint \vec{E} \cdot d\vec{l} = -\int \frac{\partial \vec{B}}{\partial t} \cdot d\vec{A}, \quad (18)$$

where the integral of the electric field is defined along the contour of the surface integral enclosing the magnetic field. The left hand side is exactly the definition of the potential of the electric field, the voltage, and since the time derivative is a partial and can be taken outside of the right hand integral, $\frac{\partial}{\partial t} \int \vec{B} \cdot d\vec{A}$, the right hand side is the time derivative of the flux of the magnetic field (Φ) through the area enclosed in the surface integral. Using Ohm's Law [2], $\epsilon = IR$, and substituting in the relation for resistance in nearby metal conductors which depends on the resistivity, a general property of the type of the material, and the cross sectional area and length $R = \frac{l\rho}{A}$ I arrive at the expression,

$$I = -\frac{A}{l\rho} \frac{d\Phi}{dt}, \quad (19)$$

which states that for a magnetic flux that changes with time, current will be induced in nearby conductors, and these are referred to as 'eddy¹ currents', and are generally short lived and small in magnitude. However, as described previously and as can be seen in Fig. 5, the stainless steel chamber is large, 12" in diameter, and a length of 18" is enclosed from the side of the coils parallel to its length and there is a lot of material in which eddy currents are generated. As seen in the previous section studying the properties of the DC magnetic field, it is clear that $|\vec{B}| \propto I$ and these eddy currents will prevent fast shut-off and turn-on of the magnetic field.

4.2 First Experimental Findings

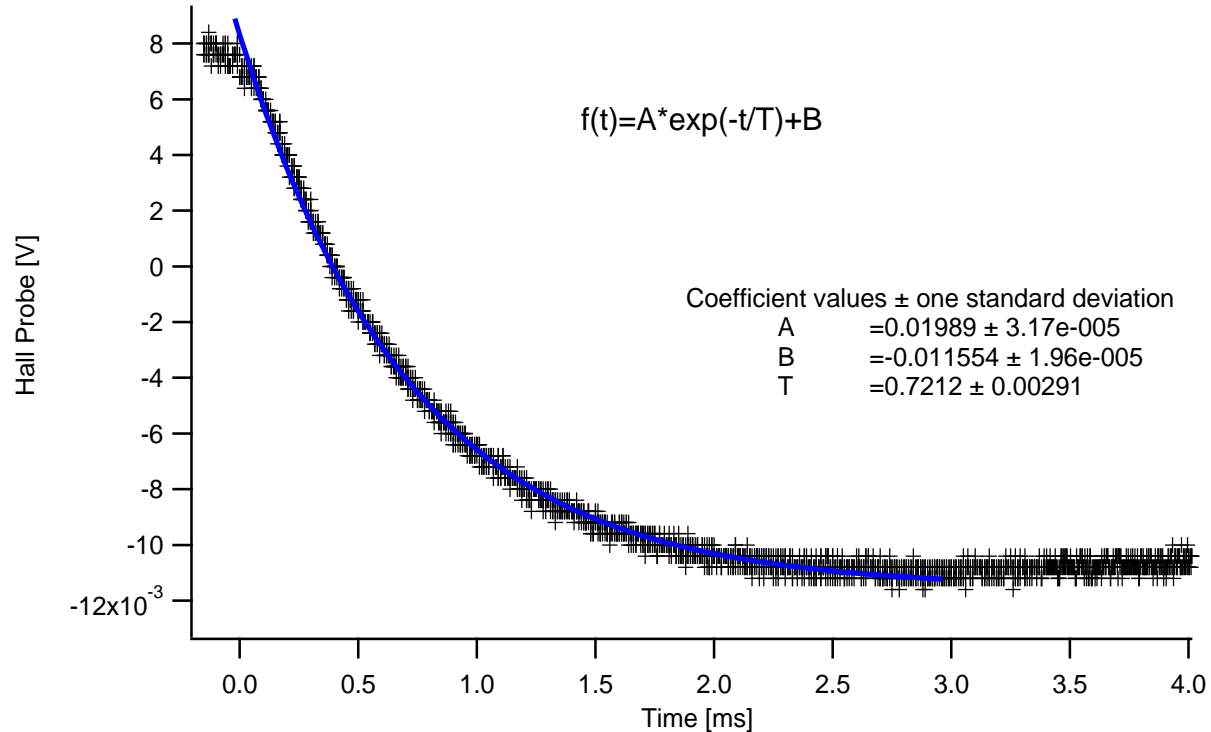


Figure 12: The first look at the decay of the magnetic field using a function generator outputting a square waveform to a Russian Coil Driver.

As shown in Fig. 12, using a basic square-wave as the logic signal to turn on and off the coils, the large chamber area, and large amount of material resulted in an extremely slow decay time, a decay constant of about $\tau = 721\mu s$. I hooked the magnetic field Hall probe to an oscilloscope in order to record the timing precisely. During calibrations I found that a 1.3G field registered as $8.51 \times 10^{-3} V$ on the Hall probe. As an aside, I used the Tenma DC power supplies to measure the background and total field on the probe such that I could convert the Hall probe signal, reported in volts by the oscilloscope, to usual magnetic field units. As I ended up analyzing a very large number of scenarios and data sets, I have decided to leave out the conversion factor as it will be easy for the reader to see by eye when the field has decayed to the background.

There are a few points I will make about the equipment used in the first experimental scenarios. The Russian Coil Drivers, designed and built at Triumf, are high voltage power supplies capable taking a logic input from a function generator and applying a large range of positive voltage. They have a useful feature of being able to apply a boost pulse that is fixed in magnitude but the duration of which can be controlled by the operator via a dial on the front panel. This feature is helpful in boosting the coils to the value of current

¹"Eddies in the space-time continuum."
"Er, who is Eddy, then, exactly?"

we wish to operate at for generating a DC field for the $1ms$ on period. However, they lack the ability to apply a negative voltage which I will explain the importance of further along in this section. The first tests I made were to see if I could decrease the fall time of the magnetic field by studying the inductive properties of the coils, and whether anything besides the chamber was effecting the field decay. Obviously, for an off period of $1ms$, $721\mu s$ was not an acceptable fall time for the magnetic field. I obtained experimental data for scenarios with and without the mu-metal present, with and without 6" copper seals placed on the outside of the chamber (these are used on the experimental chamber to vacuum seal the flanges on entry ports), placing an aluminum breadboard parallel and perpendicular to the Hall field probe, and varying the number of turns of wire. The mu-metal and copper cannot be altered on the main experimental chamber as they are needed there for magnetic shielding and vacuum sealing, but being magnetic material, I was interested in seeing how this effected the eddy currents. The aluminum breadboard was a test of conductors being parallel and perpendicular to the field, as equation 18 states, the eddy currents are dependent on the dot product (the orthogonality) of the conductor material to the magnetic field. Lastly, in most literature inductance is usually seen as proportional to the number of turns squared, N^2 and I wanted to verify whether changing the number of turns reduced the decay time. As presented by [7], the inductance from a pair of Helmholtz coils is,

$$L = N^2 r \mu_0 \left[\ln\left(\frac{16r}{a}\right) - 2 \right], \quad (20)$$

where N is the number of turns, r is the effective coil radius (half the side length if the coils are square), and a is the diameter of the bundle of wire turns. As I will show in the following section the decay constant is directly proportional to the inductance. I will summarize the effects of each scenario on the decay constant in the following table.

Scenario	Result
Added mu-metal	$\tau = 1.06\tau_0$
Added copper seals	$\tau = 1.08\tau_0$
N dependence	$\tau \approx \frac{1}{4}N$
Aluminum board $_{\perp}$	$\tau = 1.93\tau_0$
Aluminum board $_{\parallel}$	$\tau = 1.01\tau_0$

Table 1: Summary of the experimental findings for the magnetic field decay constant as various parameters are modified.

In summary, the decay time was not effected much by the presence of mu-metal or copper seals, which is somewhat expected as they are far from the center of the chamber, and are relatively small amounts of material. The aluminum breadboard, about $4x8$ ", placed inside the chamber behaved as expected when rotated with respect to the coil and Hall probe axis. The very small dependence on the number of turns was unexpected and lead me to believe that the chamber was having a dominating effect. All inductance measurements, notes summarizing the results, .csv files obtained from the Hall probe, and corresponding physica codes used to analyze the magnetic field decay and extract the decay constant can be found in the folder Documents/Ben Sheldan/Induction Measurements found on the blue HP notebook or backed up on **trinat@trcomp** in the folder bsheldan. That folder is further subdivided into sections based on the types of tests and before and after testing AC versus DC coupling of the Hall probe to the oscilloscope. In the next section I will discuss some of the mathematical modeling I did of the eddy current problem, what conclusions I came up with, the steps I took to attempt reducing the decay time, and the next lump of experimental results.

4.3 Circuit Analysis

The first loop is for modeling the coils where R_c is the internal resistance of the copper wires which was measured to be about 0.4Ω per coil, and L_c is the inductance of the copper wire. An online calculator [8] that assumes straight wire and requires an input of frequency, length, and wire gauge reports an inductance of around $50\mu H$. If the secondary loop is ignored the coils form a simple RL circuit (I have neglected the mutual inductance of the coils as it is negligible).

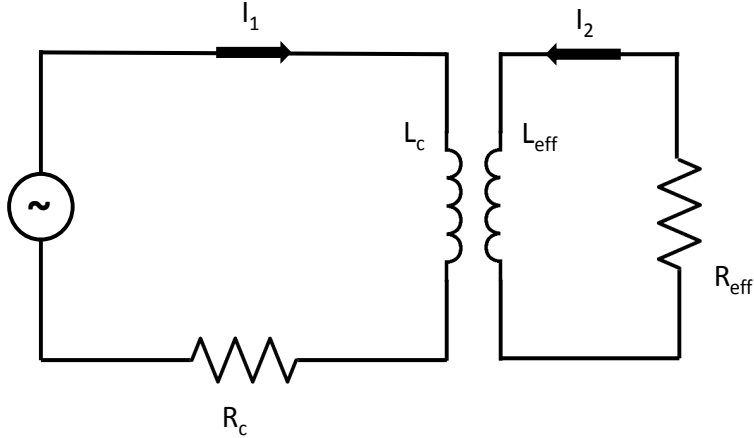


Figure 13: The circuit I used to model eddy currents induced in conductors near the magnetic field coils.

When the supply, in my case the Russian Coil Driver triggered by the logic output of the function generator, is turned off I can use Kirchoff's rule [9] to write,

$$L_c \frac{dI_1}{dt} + I_1 R_c = 0, \quad (21)$$

and solving this basic first order ODE results in,

$$I_1 = I_0 e^{-t/\tau}, \quad (22)$$

where I_0 is the initial current at $t = 0$ and the decay constant τ is defined as $\tau = \frac{L_c}{R_c}$. As the magnetic field is directly dependent to current, it follows that the same properties hold for the magnetic field generated by the coils, $B = B_0 e^{-t/\tau}$. Using the reported inductance, and the measured internal resistance of the coils, I expect to see a decay time of around $65\mu s$ for the coils only.

As is clearly shown in Fig. 14 the decay time from the coils alone is extremely quick and is close to the roughly predicted value. Without the steel chamber in the system, there were several effects I was able to verify. Inductors add by the same rules as resistors in circuits [9], $L_{tot} = L_1 + L_2 \dots + L_n$ in series and $\frac{1}{L_{tot}} = \frac{1}{L_1} + \frac{1}{L_2} \dots + \frac{1}{L_n}$ in parallel, by looking at the decay time when the coils are connected in series versus parallel to the Russian Coil Drivers, I expect to see the decay time change by a factor of 4. Small differences may be explained in the fact that the rules for adding inductors are only valid when there is zero mutual inductance and the inductors are magnetically isolated from one another. In his report on a similar study, Ian Vollrath [10], noted that by measuring the fall time of the coils in Helmholtz and anti Helmholtz alignment, one can determine the mutual inductance of the coils. By taking into account the mutual inductance and including this term in the ODE, 21, the decay constant for Helmholtz alignment is found to be $\tau = \frac{L_1 + L_2 + 2M}{R}$ and for anti Helmholtz to be $\tau = \frac{L_1 + L_2 - 2M}{R}$, and the mutual inductance can be calculated by comparing the decay measured for both scenarios. Ian's report explicitly shows that this the mutual inductance of the coils is indeed a negligible effect on the system. In table 2 I summarize my experimental findings for tests performed without the chamber present.

In summary, the results displayed in table 2 are expected. With the chamber removed the experimental results verify the rules for adding inductors in series. The factor is not quite 4, but as explained, there is a small mutual inductance, and the coils are mounted on aluminum posts so there is still metal present for induced eddy currents to be created in. Also, the Helmholtz versus anti Helmholtz test verify that the mutual inductance is small and I was able to see an N^2 dependence in the decay time once the chamber was removed. Since basic physical assumptions are valid without the chamber, it tells me that the dominating effect on the eddy currents is the chamber. As an aside, Ian did not notice these effects as his report focused on studying the anti Helmholtz MOT coils that reside within the chamber. The fact that the chamber, a large amount of conductive metal, is *within* the region of strong magnetic field, I see a large dependence on the presence of the chamber.

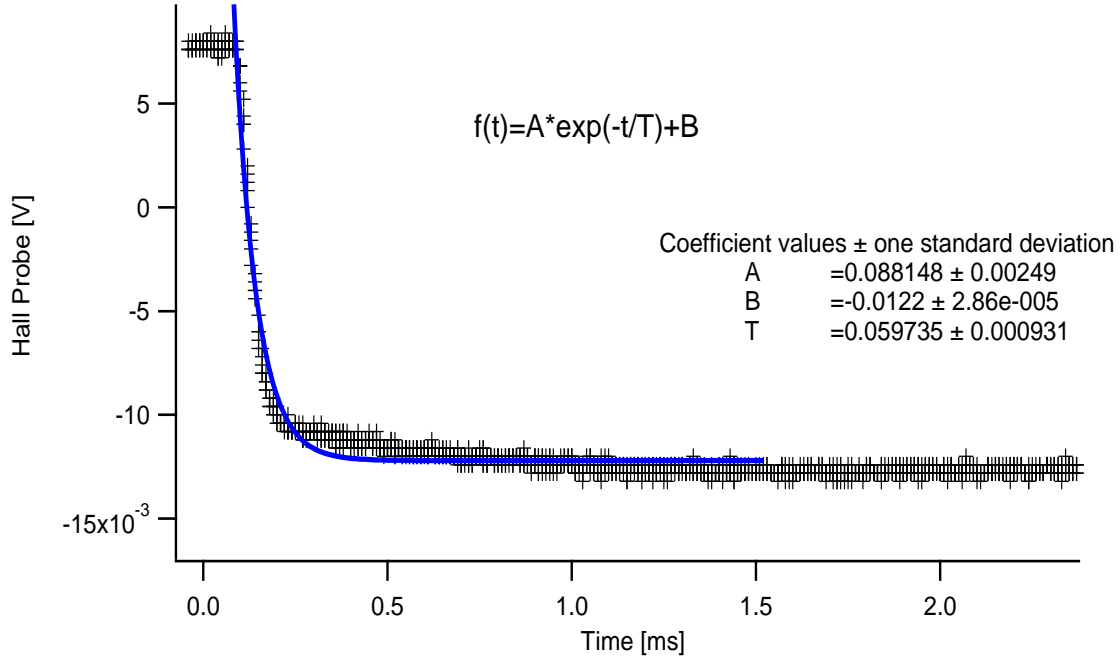


Figure 14: Decay of the magnetic field with the stainless steel chamber removed from the system.

Scenario	Result
Series vs parallel	$\tau_s = 3.35\tau_p$
Helmholtz vs Anti-Helmholtz	$\tau_h = 1.15\tau_{a-h}$
N dependence	$\tau \approx \frac{1}{2}N^2$

Table 2: Summary of the experimental findings for the magnetic field decay constant as various parameters are modified with no chamber present.

If I now consider the second loop in Fig. 13, which is used to represent nearby conductors, where R_{eff} is the effective resistance of the loop, derived from the resistivity of the material and L_{eff} is the effective inductance, I can write down a differential equation for the decay of current in each loop.

$$L_c \frac{dI_1}{dt} + k\sqrt{L_c L_{eff}} \frac{dI_2}{dt} + I_1 R_c = 0, \quad (23)$$

for the coil loop where k is the coupling coefficient determining the strength of coupling between the inductors and,

$$L_{eff} \frac{dI_2}{dt} + k\sqrt{L_c L_{eff}} \frac{dI_1}{dt} + I_2 R_{eff} = 0 \quad (24)$$

for the loop modeling nearby conductors. Here I_2 represents the eddy currents flowing in the material which can be calculated from equation 19. The first thing to note is that the two circuits are coupled and the coupling depends both on the inductance of the coils and nearby conductors as well as a coupling coefficient which is normally experimentally determined and depends on the distance between conductors and their relative geometries. In general, solving these coupled differential equations would lead to an exponential decay for the magnetic field where the decay constant, τ_{total} , will be a complicated expression involving the coupling coefficient, decay constant of the coils and decay constant of the nearby conductors, $\tau_{total} = \tau_{total}(\tau_c, \tau_{eff}, k)$. Because the systems are coupled, eddy currents will continually be produced in the chamber as long as there is current running in the coils. As I have shown in Fig. 14, appreciable values of current continue to flow in the coils for up to $50\mu s$. Decreasing this was simple, I soldered two 1Ω , $25W$,

power resistors together and secured them in a grounded aluminum box to add to the circuit and utilized an existing 0.5Ω equivalent power resistor box to increase the overall resistance in my circuit to an overall 3.3Ω . However, with the chamber added back in place, this only had the effect of reducing the decay constant to a nominal value of around $570\mu s$. Which leads me to the following section, where I implement a suggestion by a previous co-op student, Liam Lawrence, of deliberately overshooting with the logic waveform that drives the circuit in order to induce eddy currents in the opposing direction causing cancellation and decreasing the time taken for the field to decay. In the following section I will describe my work done creating a usable waveform, using both an audio amplifier and Kepco Bipolar power supply in order to drive the waveform, and how you can design your own arbitrary waveform using the software available with the BK Precision function generator, and the end results.

5 Waveform Design and Tests

5.1 Audio Amplifier

As Liam suggested in his report [11], on page 30, a deliberate overshoot of the waveform driving the coils would induce eddy currents in the opposing direction in nearby conductors leading to cancellation and a faster decay of the magnetic field. For a square waveform, this would mean generating a rectangular negative pulse to some negative voltage, $-V_0$, for a duration, Δt , that would optimize τ to be the minimum possible value. When I first thought about implementing this idea, the available Kepco Bipolar power supply was being repaired by a technician at Triumf (a fried power resistor was preventing negative current and voltage on the supply). For preliminary test of whether altering the logic waveform could be used to decrease the eddy current, I used an audio amplifier. The audio amplifier was connected to the magnetic field coils by means of a simple banana plug connection.

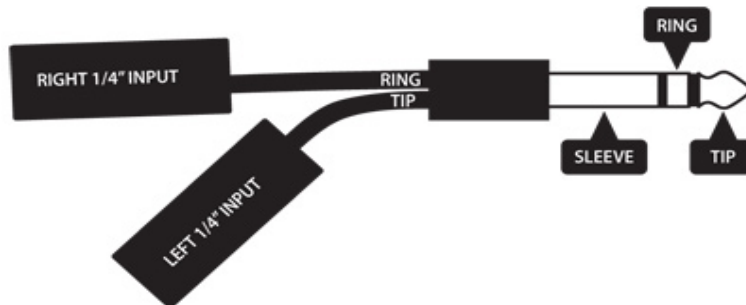


Figure 15: Tip, ring, and sleeve connections for an audio amplifier.

In Fig. 15, the tip, ring and sleeve correspond to positive (+), negative (-), and ground, respectively. By securing isolated wires to the tip and ring and using a BNC attachment to the function generator, I was able to send the logic waveform through the audio amplifier and to the coils. The audio amplifier was necessary to provide gain in order to see a large enough field (around $1.5G$). Also, some online manuals suggested tying the negative lead and ground together when only one signal is used, and I tested both ways and saw no difference in quality of signal with respect to noise so I left the ground unattached. Another feature of note is that the audio amplifier does not allow DC offsets, and for its intended purpose this makes sense, but forced my initial waveform tests to be somewhat convoluted. Basically, when a signal passes through the amplifier, if the average,

$$V(t)_{avg} = \frac{1}{b-a} \int_a^b V(t)dt, \quad (25)$$

is non-zero the internal circuit will attempt to subtract off the effective DC offset. The easiest way around this was to design a waveform with the qualities I wanted and invert it such that $V(t)_{avg} = 0$. After determining that the method would work, I would move on to use the Kepco Bipolar supply.

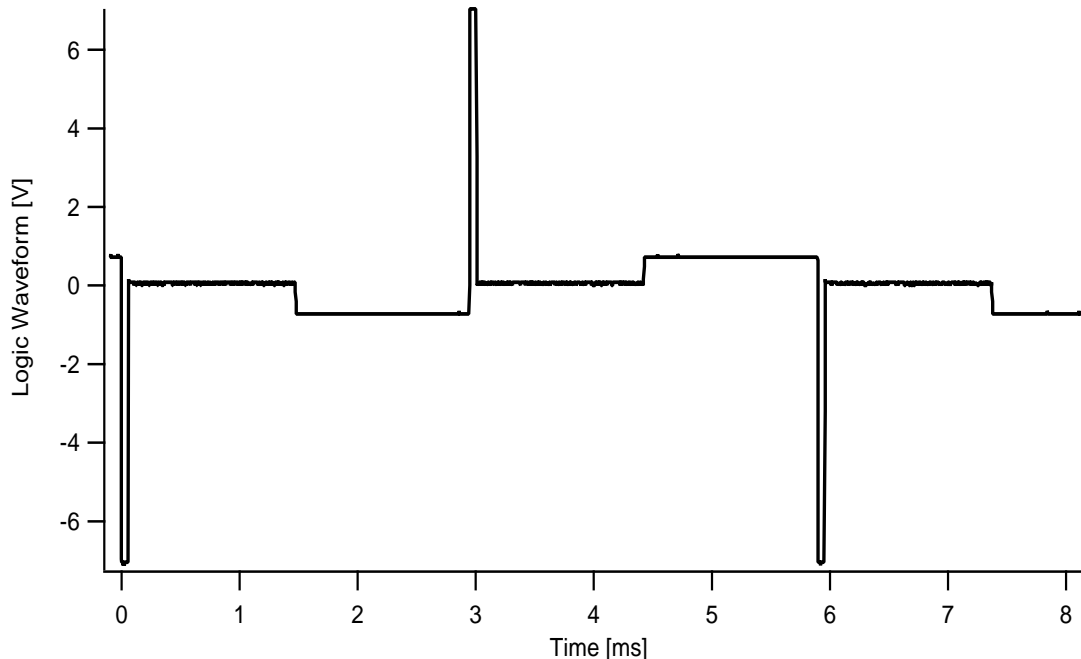


Figure 16: A typical example of the waveform I used to drive the coils via the audio amplifier that required me to invert my waveform.

In Fig. 16 I show a typical example of the type of waveform I was using to test sending the audio amplifier. It is a regular square wave with a short duration, large amplitude, negative pulse in order to quickly induce opposing eddy currents in the chamber. I tested various amplitudes and durations in order to get the quickest possible exponential decay of the magnetic field. All tested waveforms are documented in the Documents/Ben Sheldon/New Waveform folder in various subfolders corresponding to certain tests such as adding the resistor, calibrations, inside versus outside the chamber. All subfolders have their own notes.txt file. However, as the Kepco supply was going to permanently run the waveform which would no longer be inverted, these waveforms are relatively useless aside from these preliminary test I performed. I also ran into some problems with the Hall probe. For the these large pulses, the Hall probe showed extremely large spikes in the magnetic field. They were also the opposite sign you would expect if they were true magnetic field field measurements. I tested moving the wires that connected the Hall probe to the supply nearer to the coils and the noise increased. It was also visible when the probe was turned off (or not connected to power before I switched to battery to reduce AC noise). Also, when a mu-metal shield was placed around the probe and the field was shown to decrease, these spikes remained. In conclusion I ruled these out as electrical noise, but it made analysis of the fall time somewhat problematic. In the following table I report on some of the experimental findings for various modifications to the arbitrary waveform I designed as well as how the fall time improved after adding the equivalent 2Ω power resistor in series in my circuit.

Waveform	Scenario	Result
Square Wave	Added 2Ω Resistor	$\tau = 550\mu s$
Arb1	$\Delta t = 50\mu s, A = -7V$	$\tau = 143\mu s$
Arb2	$\Delta t = 50\mu s, A = -10V$	$\tau^* = 102\mu s$

Table 3: Results of modifications to the waveform driving the coils and the corresponding circuit.

τ^* refers to the best value of decay constant that I was able to achieve. I did achieve better decay times than $\tau = 102\mu s$, however, these were for field values less than $1.5G$ during the “on” period, or such that the field decay to a value slightly below the measured background and I was actually putting on too long

of a pulse and inverting the sign of the magnetic field. In the following section, I will outline how to install and use the EasyWave software that came with the BK precision function generator for designing arbitrary waveforms. This will be useful if any future students need to design arbitrary waveforms for any reason.

5.2 Easy-Wave Installation and Use

Previously, Dr. Behr and I attempted to install the Windows software that comes with the Tenma power supplies on the HP notebook I have been using this term under Wine, an open source software that allows users to install and run Windows applications on Linux systems. We did not have much success and decided to use the small “Certified Data” tablet that has Windows to run the software. Using the disk that comes with the function generator, the user will be prompted to download the software when the disk is installed. After installing the program the user must go to the National Instruments website and download an additional, free, program called **visaruntime.exe**, otherwise the program will not run (I’m still mystified as to why this program is required and not included on the disk, but it was easy to find). An EasyWave icon will appear allowing the user to start the program. When opening the program, the user is prompted to create a new waveform and is able to select a period or frequency and number of points and after selecting these, a blank graph is displayed. There are multiple ways for the user to create their own arbitrary waveforms.

1. First, there are several built in “arbitrary” waveforms such as decaying and growing exponentials, various step functions, a sinc function, and other sinusoidal waveforms. These are available from a menu on the left.
2. The second is via a mathematical equation. If the desired waveform is continuous, the user can type an mathematical expression and generate a plot of the waveform. As a side note, all variables must be declared. For example, ax^2 would not be permitted unless you declared a to be a specific value, ie $a = 2$.
3. The third method is via hand draw. The hand draw mode allows the user to drag a pointer around screen to draw a waveform, much like free hand drawing in the MS paint application. This is usually messy as the tablet is small, but would be inaccurate regardless. However, I found it useful for quickly generating waveforms when attempting to roughly estimate some parameters. More refined methods can follow after using the freehand tool.
4. Next, there is line draw. Using line draw, the user can draw horizontal or vertical lines. Much like free hand, this method is not extremely accurate, but does eliminate one degree of freedom making it easier to draw semi accurate square-like waveforms. Again, this method is easy and helpful to use when roughly determining parameters.
5. Lastly, there is coordinate draw. This method allows the user to select the number of points they wish to enter, and specify an amplitude for each time. If no amplitude is mentioned for a given time, the program will automatically connect them with a straight line. This is useful if your waveform is constant for a duration as you need only specify the end points. As a side note, the steepest slope I was able to create when designing a waveform was a slope of 10V over several nanoseconds. Attempting to specify a steeper slope on the edge of a square wave results in the program giving you 0 for the desired amplitude there.

All waveforms are saved as comma separated value (.csv) files. If the user desired, these can be modified separately and reloaded to display the new waveform. Once the user has created a waveform, it is time to send it to the function generator. Connecting the tablet and function generator via USB (standard to type B connection), the user can select the “send wave” option in the menu, which will prompt naming the wave and selecting a storage slot on the function generator. Up to 10 arbitrary waveforms can be installed on the function generator at one time and previous waveforms can be overwritten if desired. The waveforms can be accessed from the “arbitrary waveform” menu option on the function generator, and the user can scale the amplitude and period, as well as set a DC offset on the arbitrary waveform.

As mentioned, the issue with using the audio amplifier to drive the waveform was having to invert it, which was unnecessary and not desired for the coils. The Kepco Bipolar supply was our main option for

permanently driving these coils, and once it was available, I began testing with it. The audio amplifier had been useful in showing that this was a reliable method for reducing eddy current effects from the chamber. However, as the Kepco only had a possible $\pm 75V$ range compared to the $\pm 150V$ range I had been using on the amplifier, the waveform needed tweaking. Also, the Russian Coil Driver had been providing a boost pulse to quickly get the field up to the value we desired during the “on” time. As the Kepco lacked this feature, I would need to add my own boost pulse to the logic signal, otherwise the rise time for the field would be similar to the fall time of the original square wave logic signal (close to $750\mu s$).

5.3 Kepco Bipolar Supply

I used EasyWave once again to design a final waveform that the Kepco would be able to drive. In the arbitrary waveform design, I applied a $-10V$ overshoot pulse for a duration of about $275\mu s$ in order to induce opposing eddy currents for cancellation and increasing the fall time and a $+10V$ boost pulse for a duration of $350\mu s$ for fast turn on of the magnetic field. During the “on” portion of my wave where the magnetic field is essentially constant with time, the arbitrary waveform design was set to around $4V$. I used the amplitude scaling on the function generator itself while collecting data to fine tune the amplitude to achieve the field strength desired at the center of the chamber. Below, in Fig. 17, I display the final decay curve of the magnetic I achieved with the Kepco Bipolar supply. The cancellation of eddy currents was not quite linear with respect to amplitude and time duration in a sense that a pulse, for $-150V$, $50\mu s$ with the audio amplifier, did not correspond to the same fall time of a pulse of $-75V$, $100\mu s$ with the Kepco Bipolar supply. This could be due to a difference in effective impedance of the circuit as the supplies could contribute differently. To calculate the total impedance of a circuit,

$$Z^2 = R^2 + X^2, \tag{26}$$

where Z is the overall impedance, R is the resistance, and X is the net reactance, one must take into account the resistance as well as the magnitude of the reactance from components such as inductors and capacitors. The audio amplifier had a spec given for its impedance at given frequencies but I did not find one for the Kepco. However, from Fig. 17, a final fall time of $\tau = 241\mu s$ was usable for our purposes.

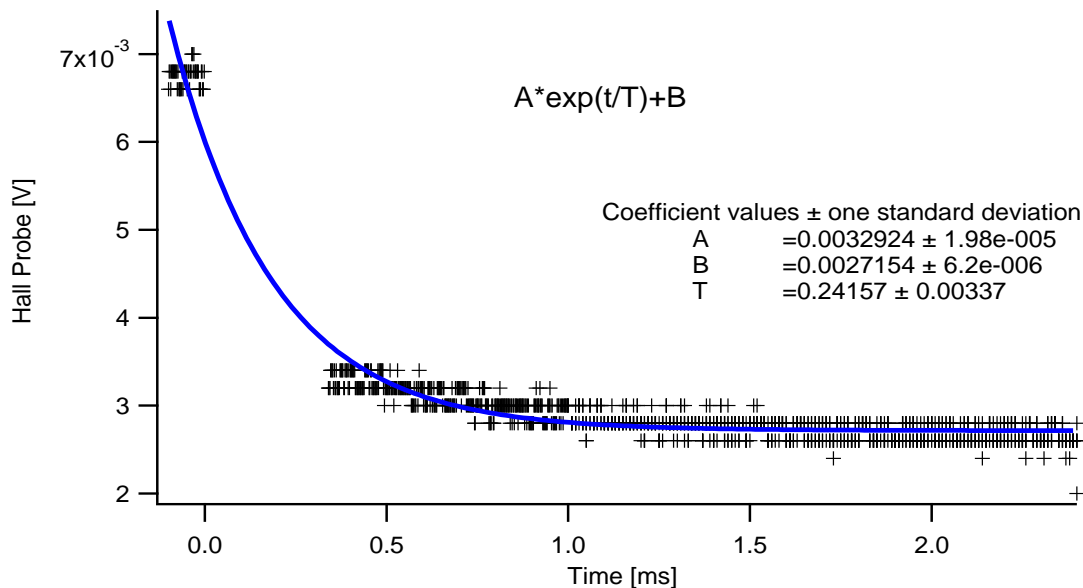


Figure 17: The final decay curve corresponding to the logic waveform in Fig. 18 with electrical noise removed.

In summary, there were various unforeseen problems with the fast turn on and shut off of these trim coils. Although the nearby conductors were non magnetic, with relatively high resistivity, the large amount of material lead to the production of large amounts of eddy currents. Also, previous work such as Liam’s

and Ian's, which were also concerned with fast shut off of coils had the difference of being placed within the chamber. When the coils are placed inside the chamber, the effective coupling of the inductors (see previous circuit diagram) would be much smaller as the field decays faster beyond the coils. The magnetic Hall probe also showed lots of electrical noise when adding the necessary pulses to the arbitrary waveform. In the /Documents/Ben Sheldon/New Waveform folder, I have saved pictures of the oscilloscope display showcasing the electrical noise with and without the mu-metal shield in place around the Hall probe. There was a secondary Hall probe, however, it had a large DC offset that would not allow it to be seen on the oscilloscope when DC coupled. Despite these problems, I was able to design and test arbitrary waveforms using several supplies, a Russian Coil Driver, audio amplifier, and Kepco Bipolar supply, and reduce the fall time from $770\mu s$ to $233\mu s$. Using the boost pulse, I stabilized the field during the “on” time. The only things left to consider before adding to the permanent setup would be how many turns of wire we desired for the required field strength (I have shown that with the chamber in place, the decay time τ only weakly depends on N , not N^2 and with some tweaking, the waveform would work for a higher N) as well as detector shielding, which I will discuss in the following section.

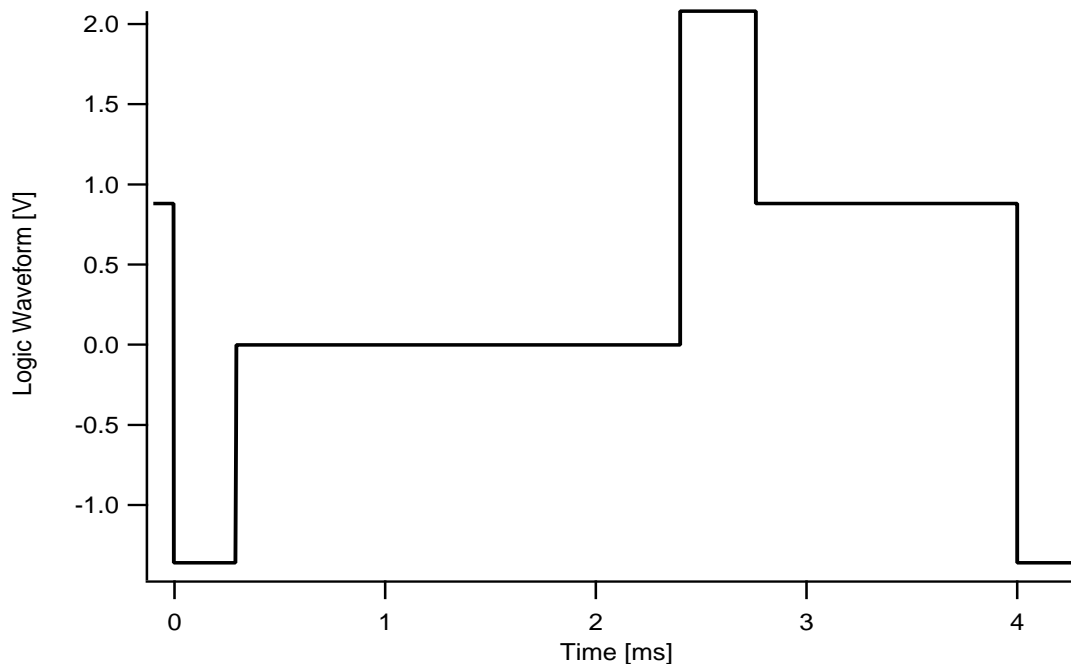


Figure 18: The final waveform I designed to be run by the Kepco Bipolar power supply.

One final note is for testing during the “on-line” setup of the main chamber. Since the chamber is vacuum sealed I wanted to find a location outside the chamber that would allow me to model the decay time for the magnetic field at the center of the main chamber without having to open it. I found that by placing the probe in the xz -plane at y positions $\pm 15.2cm$ (directly against the chamber, oriented along the coil axis) I could observe the decay of the magnetic field here and relate it to the decay of field at the center of the chamber. Refer back to Fig. 5 for axes definitions. For the same waveform the decay of the field outside the chamber could be modeled with,

$$B(t) = A\cos(\omega t + \phi)e^{-\frac{t}{\tau_{out}}}, \quad (27)$$

and I could place an upper limit of the corresponding decay constant inside the chamber (τ_{in}) as $\leq 1.33\tau_{out}$. All files for this analysis may be found in the folder /Documents/Ben Sheldon/New Waveform/Inside vs Outside as well as notes and corresponding physica scripts.

6 Photomultiplier Tube (PMT) Shielding

Since my coils are much larger than the current AC-MOT coils inside the chamber, as well as placed outside rather than inside the chamber, there will be a magnetic field created on the outer edges of the coils, closer to the PMTs. PMTs are sensitive pieces of equipment used to detect extremely weak signals, such as those from a single photon. In the TRINAT lab, PMTs are placed directly above and below the main trap chamber (see the following, Fig. 19) along the vertical axis.

As previously mentioned, the spin polarization of the parent nucleus allows for precise prediction of where the decay products will be located. β^+ particles, positrons, are antimatter particles that annihilate upon contact with matter and produce energy (photons). The basic way the PMT works is that the oncoming incident photon knocks an electron off of the photocathode as a result of the well known phenomena, the photoelectric effect. This electron, referred to as the primary electron, is focused to the first dynode (an electrode in vacuum) and is accelerated such that it kicks off multiple electrons at subsequent dynodes. This avalanche effect multiplies the signal and is read out at the end by hooking the connector pins to data acquisition hardware and a computer for processing.

However, one issue with these types of detectors is that they are susceptible to gain loss if placed inside a magnetic fields. From the Lorentz force,

$$\vec{F} = q\vec{v} \times \vec{B}, \quad (28)$$

where \vec{F} is the force, \vec{v} is the velocity and \vec{B} is the magnetic field, charged particles are deflected by magnetic fields. Photoelectrons can be deflected such that they miss the dynode and signal will be lost. This is not much of an issue near the end of the PMT as the signal has been amplified, but it is critical that the primary electron not be deflected from hitting the first dynode.

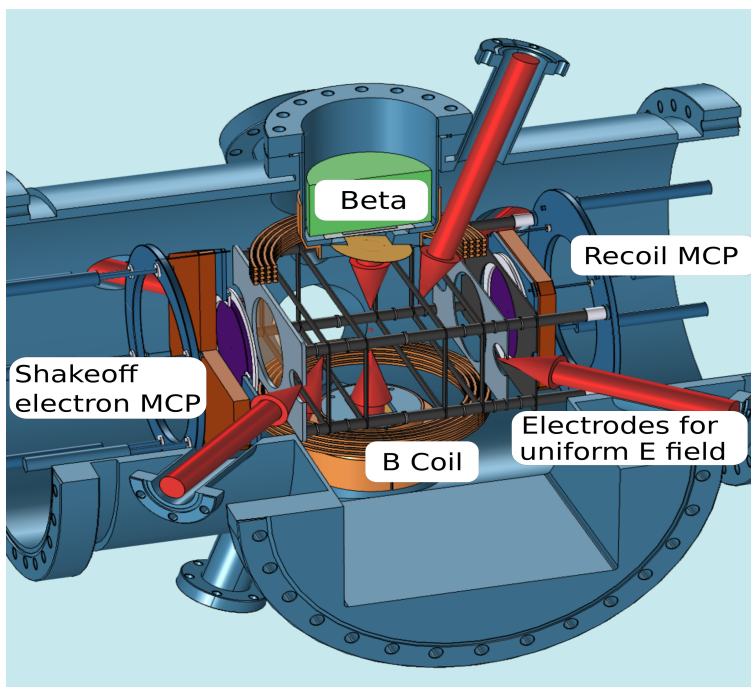


Figure 19: Diagram of the main trap chamber depicting the shakeoff electron and recoil nucleus microchannel plates, AC-MOT coils, and laser paths [12].

Previously, the coils creating the quadrupole field inside the main trap chamber are quite small, as well as closer together. As presented earlier, I have shown that the magnetic field strength from a circular loop of coil falls off as $\frac{1}{z^3}$, where z is along the coil axis, such that the field will have decayed by a large amount near the front end of the PMTs. And for added protection, a single layer of Co-Netic mu-metal [13] was added as magnetic shielding. The additional rectangular coils to be added to the chamber are both larger and closer

to the PMTs, and consideration on how to reduce the magnetic field at the front end of the PMTs was required. There are modernized silicon detectors which are insensitive to magnetic fields which would work great for this scenario, but the replacement of sensitive detectors would be a much more involved job than the remaining time in this co-op. In addition, these detectors are quite expensive and I needed to find an alternative approach. As I mentioned previously, an analytic model for the current mu-metal setup, as well as the field coils would be difficult to write down. When I compared the experimental magnetic field results with Alexandre, a senior member of TRINAT who used COMSOL to model the system, and when modeling the eddy current effects, he had to resort to a spherical shell rather than cylindrical to obtain timely results. This prompted me to do the same for the eddy current system. I wasn't necessarily interested in exact expressions, although after this analysis obtaining those analytically is possible, but rather what could effect the field inside the PMTs. From the following, Fig. 20 [13], the material is shown to saturate for low fields (in vacuum, an Oersted is equal to 1G), and the field inside may depend on the thickness of material as well as additional layer. It would obviously also depend on the permeability itself, but also possibly the radius although a smaller radius would be impossible to implement on the main chamber as the shielding is fixed around the scintillator and PMT.

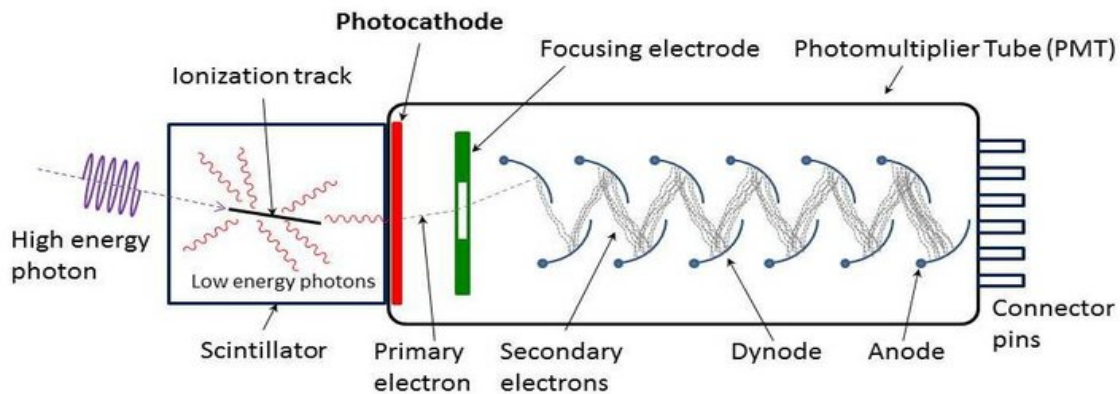


Figure 20: Schematic of the incident photons, scintillator light, primary photo-electrons and dynodes in a photomultiplier tube (PMT). [18]

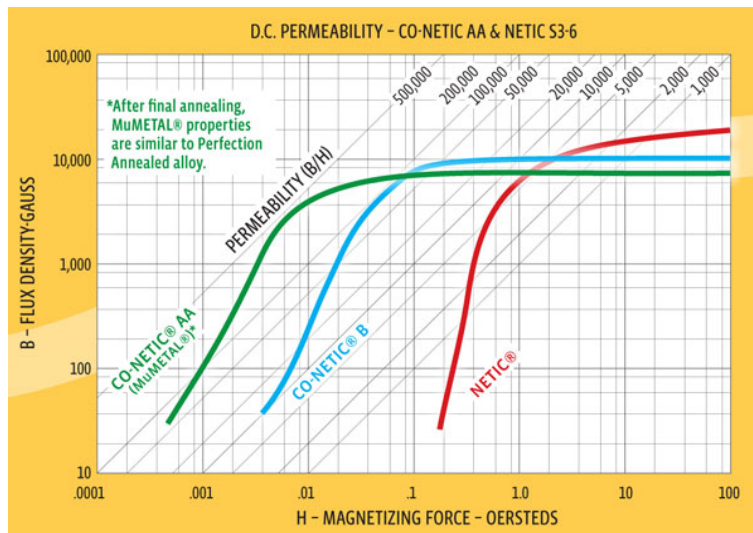


Figure 21: Curve depicting the saturation of various magnetic shielding materials obtained from the commercial company, Magnetic Shield Corp., where TRINAT purchased their mu-metal [13].

To test if an analytical model for this scenario was possible, I considered placing a spherical shell of mu-metal inside a uniform magnetic field, refer back to Fig. 9, to see what factors the field within the shell depended on. Let the sphere of mu-metal have an inner radius a , outer radius b and thickness δ . Let the magnetic field be described by $\vec{B} = B_0\hat{z}$. In the absence of free currents, for a magnetic field constant in time (the mu metal has a high resistivity and there is little material there, and as proven earlier, does not contribute much to eddy currents) I can write [2],

$$\vec{\nabla} \times \vec{H} = 0, \quad (29)$$

where \vec{H} is the usual auxiliary field and using the vector calculus identity, $\vec{\nabla} \times (\vec{\nabla}\phi) = 0$, that the curl of a gradient is zero, then I can write the auxiliary field \vec{H} , as a the gradient of a scalar ϕ where $\vec{H} = -\vec{\nabla}\phi$ and the minus sign is added simply as convention (think of the regular scalar potential everyone is familiar with from electrostatics). The magnetic field \vec{B} and auxiliary magnetic field \vec{H} are related by $\vec{B} = \mu\vec{H}$, where μ is the permeability. Using one of Maxwell's equations again, $\vec{\nabla} \cdot \vec{B} = 0$, and substituting the relation between the magnetic and auxiliary field I end up with Laplace's equation,

$$\vec{\nabla}^2\phi = 0, \quad (30)$$

which is a second order PDE. A sphere demands that I adopt spherical coordinates and I can eliminate the azimuthal angle as the problem is symmetric as we rotate around the azimuthal angle which leads to [14],

$$\frac{1}{r^2} \frac{\partial}{\partial r} (r^2 \frac{\partial \phi}{\partial r}) + \frac{1}{r^2} \frac{1}{\sin(\theta)} \frac{\partial}{\partial \theta} (\sin(\theta) \frac{\partial \phi}{\partial \theta}) = 0, \quad (31)$$

where r is the radial coordinate and θ is the polar angle and this can be solved using separation of variables. By assuming $\phi(r, \theta)$ can be written as the product of two single variable functions and substituting,

$$\phi(r, \theta) = R(r)\Theta(\theta), \quad (32)$$

and multiplying equation 30 by $\frac{1}{\phi}$ we can see the result is,

$$\frac{1}{R} \frac{1}{r^2} \frac{d}{dr} (r^2 \frac{dR}{dr}) + \frac{1}{\Theta} \frac{1}{r^2} \frac{1}{\sin(\theta)} \frac{d}{d\theta} (\sin(\theta) \frac{d\Theta}{d\theta}) = 0, \quad (33)$$

where radial and angular variables have been decoupled. Using the regular separation of variables technique that says if, $\frac{df}{dx} + \frac{df}{dy} = 0$, the condition can only be satisfied for all values of x and y if $\frac{df}{dx} = \pm k^2$, where k is a constant and a similar constraint $\frac{df}{dy} = \mp k^2$ on the other term. By setting the radial equation equal to a constant, $l(l+1)$, the well known solution is of the form [14],

$$\phi(r, \theta) = \sum_{l=0}^{\infty} (A_l r^l + B_l r^{-(l+1)}) P_l(\cos\theta), \quad (34)$$

which involves a rational function of the radial coordinate and Legendre Polynomials, special functions that satisfy the angular equation. I solved this equation for ϕ in three regions, $r < a$, $a < r < b$, and $r > b$ which result in ϕ_1 , ϕ_2 , and ϕ_3 respectively. To solve we apply the electromagnetism (EM) boundary conditions that $\mu_0\phi_1|_{r=a} = \mu\phi_2|_{r=a}$ and $\mu_0\frac{\partial\phi_1}{\partial r}|_{r=a} = \mu\frac{\partial\phi_2}{\partial r}|_{r=a}$ and the same conditions on ϕ_2 and ϕ_3 at the outer radial, $r = b$ boundary. After applying the appropriate EM boundary conditions, as well as the requirement that $\phi|_{r=0}$ and $\phi|_{r=\infty}$ are both finite, I arrive at the solutions

$$\phi_1 = \text{Arcos}(\theta), \quad (35)$$

for $r < a$, $\phi_2 = (Br + \frac{C}{r^2})\cos(\theta)$ for $a < r < b$ and $\phi_3 = (\frac{D}{r^2} - \frac{B_0}{\mu_0}r)\cos(\theta)$ for $r > b$ where I will focus mainly on the solution for ϕ_1 as I am interested in how much the field is attenuated and what factors it depends on. First, I tested that for points far from the sphere the field behaves uniformly again (as it should, the effects of the mu-metal won't be felt by the field far from the sphere). And indeed, in $\lim_{r \rightarrow \infty} -\mu_0 \nabla \cdot \phi_3(r, \theta)$, the

expression $\vec{B} = B_0 \hat{z}$ is recovered. After applying the appropriate boundary conditions, to solve for for the specific constants I can put my system of equations into matrix form,

$$\begin{bmatrix} \mu_0 & -\mu & 2\mu/a^3 & 0 \\ a & -a & -1/a^2 & 0 \\ 0 & \mu & -2\mu/b^3 & 2\mu_0/b^3 \\ 0 & b & 1/b^2 & -1/b^2 \end{bmatrix} \cdot \begin{bmatrix} A \\ B \\ C \\ D \end{bmatrix} = \begin{bmatrix} 0 \\ 0 \\ -B_0 \\ -B_0 b/\mu_0 \end{bmatrix}. \quad (36)$$

To solve this matrix equation, $A \cdot X = B$, I can take the inverse of matrix A , and write $X = A^{-1} \cdot B$ where X is my matrix of coefficients I wish to solve for. After solving for the coefficient A , taking the gradient of the potential ϕ , substituting the relations between auxiliary field \vec{H} and \vec{B} and Taylor expanding after assuming that $\delta \ll a$ and $\mu \gg \mu_0$ I end up with the expression,

$$|\vec{B}| \approx \frac{3}{2} \frac{\mu_0}{\mu} \frac{a}{\delta} B_0. \quad (37)$$

For a sealed sphere of mu-metal, the magnetic field inside will be attenuated by a high permeable material, a smaller radius, and thicker sphere.

As seen experimentally, an additional layer, separate from the initial layer also works. In the following, Fig. 22, I display the experimental data I took for the field along the coil axis inside a single layer of mu-metal shield, and the data taken when a second layer was added. In a thicker material, the material closer to the field attenuates the field, is saturated, and a weaker field continues to permeate through. The nature of the strength of the field inside the material, whether a linear, exponential, or some other mode of decay is seen most likely depends on the type of material and whether permanent magnetization (hysteresis) occurs. This means that adding layers of mu-metal will allow for increased magnetic shielding of the PMTs.

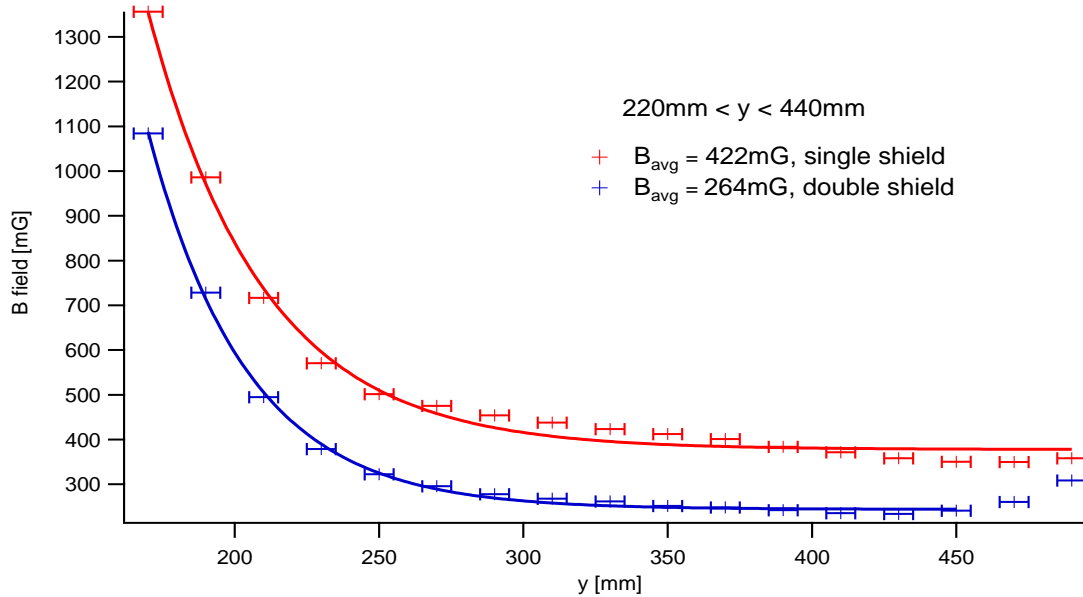


Figure 22: The attenuated field along the coil axis for a single cylinder of mu-metal and for two layers.

The reason I have taken averages at specific y locations was such that I could take the average of the field inside the mu-metal. As seen at the tail end of the two shield curve, near the edge of the mu-metal cylinder the field becomes slightly stronger again as the influence of the shielding drops. Also, I began the plot closer to the coils in a region not yet shielded by the mu-metal which should be obvious from the relative strength of the field. This solved the issue of shielding the detector. In the folder Documents/Ben Sheldan/PhotoMultiplier Tube Consideration, I have placed the .txt files for the data of the magnetic field both with and without mu-metal shielding, as well as the multiple layer mu-metal scenario, the physica

scripts used to plot the data, and notes.txt file which documents the various scenarios. In a spec found in the Useful Paper and References folder, the PMT is stated to lose 50% of its gain in a field of $800mG$ in its “most sensitive direction” [20]. I attempted to take data for the transverse field in the tube, but it was difficult to obtain reasonably accurate and reproducible position measurements and decided against taking data for these directions. I have also shown in the magnetic field sections of this report that transverse field near the coils axis are small, and they would be attenuated further with the mu-metal shielding. The data for the field along the axis is very reproducible as documented and proven in the folder noted above.

There are also other reasons than the fact that the current mu-metal shields are cylindrical rather than spherical that contribute to the actual experimentally observed degree of attenuation inside. The magnetic field is parallel to the surface of the cylinder, whereas my simplified model has mu-metal which is perpendicular to the field lines (this changes the boundary conditions slightly). There are also a number of additional factors to be accounted for when studying magnetic shielding which I will mention briefly. First, there is “magnetic conductivity” and a related resistance which can be used to define an equivalent circuit for the amount of field lines that a material can draw in. Also, there is an analogous “magnetic pressure” in which there is a limit to how close the magnetic field lines may be compressed depending on the type of material which leads to saturation. When saturation occurs depends on the flux density of the field and also the amount of shielding material and other factors such as permanent magnetization of the material. Overall, all of these factors must be carefully considered when studying the shielding of sensitive equipment and it is important to know how the model/simulation you are using takes these factors into account and whether there are limitations and when they will fail.

In the remaining sections I will discuss two slightly different topics. During my term at Triumf I helped Alexandre with the assembly of a new shake-off electron microchannel plate detector, and I will describe the basics of the theory of how they work, as well as assisting with installation in a vacuum chamber for testing and calibration. Lastly, I will discuss the new Tenma digital power supplies acquired by TRINAT, sending serial commands, implementing an automated sweep of the supplies using C++ code and how it effected the trap position and possible future work that could be done on this aspect.

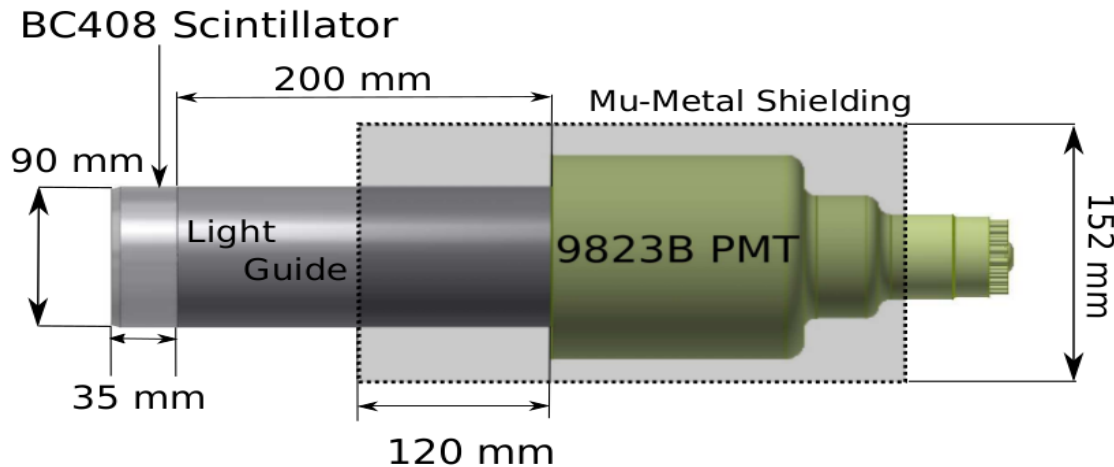


Figure 23: The diagram of the location of the PMT with respect to the scintillator, light guide, and mu-metal shielding [12].

7 Shake-off Electron Detector

The basic idea of a wedge and strip microchannel plate (MCP) detector is to have a detector with the capability of reporting position sensitive particle hits. The idea is not just to know an electron hit the plate, but where on it that it hit. The initial multiplication of the signal works on a similar principle to PMTs such that after initial contact a resulting avalanche is created. By raising the voltage to slightly different values

(200V), a potential bias between anodes is created (and the front plate is grounded) and a relatively uniform electric field is produced. The detection of the cloud image by the wedge and strip works by measuring the relative charge accumulated on each, as well as a normalizing electrode, Z. Fig. 24 shows this in further detail.

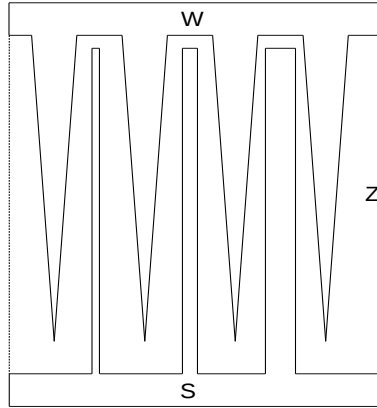


Figure 24: Diagram depicting the wedge (W), strip (S), and normalizing (Z) electrodes used in the MCP [15].

By varying the size of the strips along the horizontal axis, and wedge along the vertical, the size of the charge on each electrode will be proportional to the position of the cloud. The Z electrode is clearly in place for normalizing the amount of charge collected. Explicitly, one can write,

$$x = \frac{2Q_s}{(Q_w + Q_s + Q_z)}, \quad (38)$$

and the same equation for the y position, except in terms of Q_w rather than Q_s .

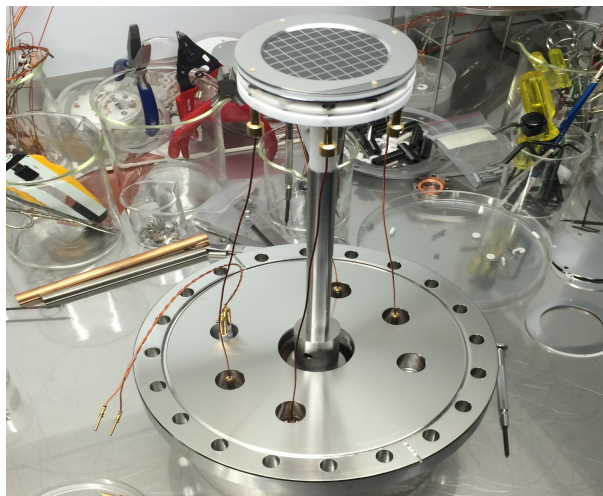


Figure 25: The electron MCP detector before installation into the vacuum chamber with α -source.

One pitfall that must be avoided is making sure that cloud size is not smaller than the thinnest strip. If this is the case, the position signal will be false and report a large signal such that it appears to have landed on the strips farther to the right. The same is true if a tiny cloud hits the tip of a wedge. In order to test and calibrate the detector, we installed it in a test chamber with a removable α -source. The detector, as shown

in Fig. 25, before installation has a mask that would clearly indicate whether we were able to determine the position of the α hits. After Alexandre and I biased the electrodes, hooked up the preamplifier and used an oscilloscope to test whether we could see pulses (we also added signal attenuators to accommodate the required pulse height required for data acquisition), Melissa and Alexandre worked on analyzing the spectrum of α particles observed, and for the initial runs we saw promising plots of position with the mask pattern easily visible.

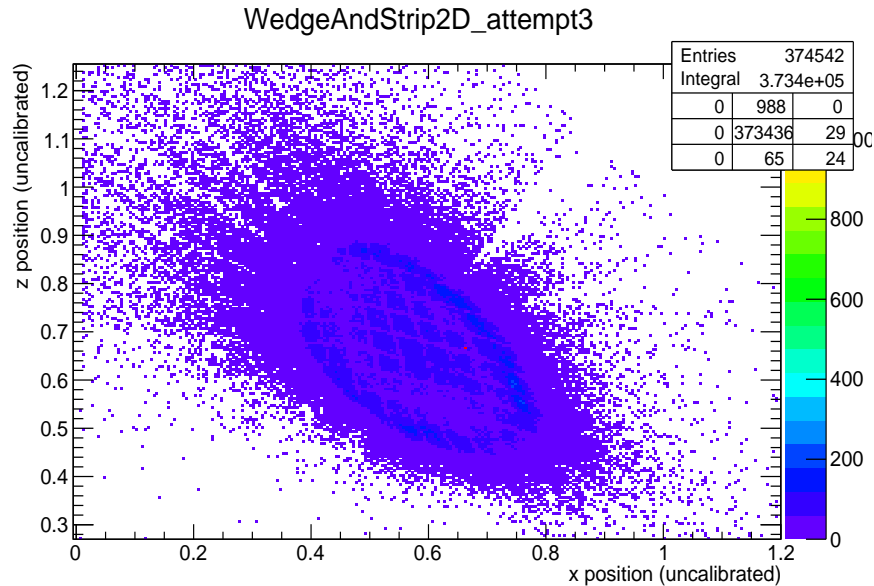


Figure 26: Initial, uncalibrated data of the position readout from the electron MCP, courtesy of Melissa.

As an aside, for data acquisition there are charge-integrated and pulse height methods. Pulse height simply looks at the maximum value seen during a certain triggered gate. The charge-integrated method looks at the area under the pulse during the triggered gate period. In both cases it is important to trigger the gate over the correct range such that the maximum pulse height, or total area is captured. For the first tests, we were required to invert and attenuate the signal as data acquisition only tolerated a certain sign and up to $400pC$ of charge. Lastly, I will discuss the sweeping of power supplies, basics of sending serial commands, using terminal emulators as well as C++ to send these commands and how I integrated these into the existing code used in the TRINAT lab for the DC trap. Also, I will give a brief overview of some of the code running, as well as how you can access, modify and add code for yourself.

8 Programming Power Supplies

There were several steps to be completed before the full plan of automating a sweep of the power supplies to optimize trap position could be implemented. Learning the basics of how serial commands are sent and how terminal emulators work in order to make sure we are sending the right commands to the supplies was necessary. I have previous experience with writing code in Matlab and Python and very basic C but learning and refreshing syntax for C was helpful, as well as studying the existing code and hardware in the TRINAT lab.

8.1 Terminal Emulators

When I first connected the power supplies and attempted to send commands, the power supplies were unresponsive despite following commands precisely as specified in their manual [16]. The first terminal emulator I used was GtkTerm, a basic program that lets you access a specific port on your computer,

configure it, and send line commands (others exist such as Moserial, Miniterm, and many more). Although GtKterm did not work for the power supplies, I was able to use a basic FTDI chip² to test and understand the emulator, and the following applies to all terminal emulators, although default settings may be different. The first step in setting up a terminal emulator is finding the configuration>port menu. From there you can select the port you wish to connect with, an example being /dev/ttyUSB0 which is a device connected to USB port number 0, and the structure of the commands you wish to send such as baud rate, parity, and more which I will explain further in the following section. To see which port a device is designated to, on Linux you can use the command `ls -l /dev` and if you have just connected it, it will be the last device listed. Similarly on Windows, you can access Device Manger>Universal Serial Bus Controllers, and expanding will have a list of connected devices the same as with Linux OS. The next step is to turn on local echo in order to see what you are typing so you don't misspell commands. On some emulators, however, it is possible that turning on local echo can send double commands such as "hheellloo" rather than the intended "hello" and it is important to test whether the emulator you are using has this problem. A simple test is to hook up a basic FTDI chip and connect its transmitting (TX) and receiving (RX) pins (so that whatever character you send is just returned back to the computer) with local echo turned off. With local echo off, you should see each character only once when TX and RX are connected, and not at all if they are disconnected. With local echo on, and TX and RX disconnected, you should see each character only once as well, as so on. Lastly, some devices require a carriage return, CR, to be placed at the end of a command such that it recognizes and confirms which segment of characters are a command. Other devices simply wait an allotted time in between receiving characters and if another character is not received within that timespan, the device interprets those as a command and it is important to check what type you device requires. The issue I saw with GtKterm is that each character was sending separately and the power supply was interpreting each character as a separate line, and obviously not responding as they were incorrect commands. For controlling the power supplies, the Moserial terminal emulator worked well as it allowed you to type your entire command into a buffer line before sending such that the device received the string without timing out. One unresolved issue, likely a fault of the supplies internally, was that they did not respond consistently when queried. One feature of the supplies mentioned in the manual was being able to ask the current it was set to, and what the actual output was. After testing multiple supplies and only receiving intermittent, inconsistent responses, I abandoned attempting to ask for feedback from the supplies. One last note is that terminal emulators require superuser privileges to write to serial or USB ports as well as access to the dialout group on the computer. To do this, on Linux OS for example, requires typing `sudo` before starting up the terminal emulator program and similar parallel steps would be required on Mac or Windows and checking for dialout access requires accessing `system>administration>users and groups`. Now that the supplies were responding to commands, the next step was to learn more about the theory of sending serial commands and how they work before learning to write code that would take the place of the terminal emulators. In the following section I will describe the basics of sending serial commands.

8.2 Serial Command Basics

In order for devices (a TX device, the computer, and a RX device receiving the commands) to swap information, they must have common communication protocol of which there are two types, parallel and series. For parallel communication protocol multiple bits are shared and sent along parallel connections and these are referred to as buses. In series a single bit is sent along one connection and each follow the other along this common path (and this is where the term serial command comes from).

As depicted in Fig. 27, there are 9 pins in the standard serial connector, only three of which are required for the most basic serial commands and they are pins 2, 3, and 5. Pins 2 and 3 are for received and transmitted data respectively, and a standard voltage (ranging several volts depending on the type of device) is sent for every data bit, with respect to the ground connection on pin 5. The baud rate is what specifies how fast data is sent over a serial line and is expressed in units of bits per second. Both devices must to set to the same baud rate to understand each other. The devices use baud rate to specify time in between voltage pulses along the TX and RX pins and if the information is sent at one speed and received at another the devices will not be to reconcile the pulsed voltages into coherent data. A package of data bits is framed by adding parity and stopping (synchronization) bits which act in a similar way to knowing that a number is

²FTDI Basic Breakout - 3.3V, Digi-key through Sparkfun Electronics (USA), DEV-09873

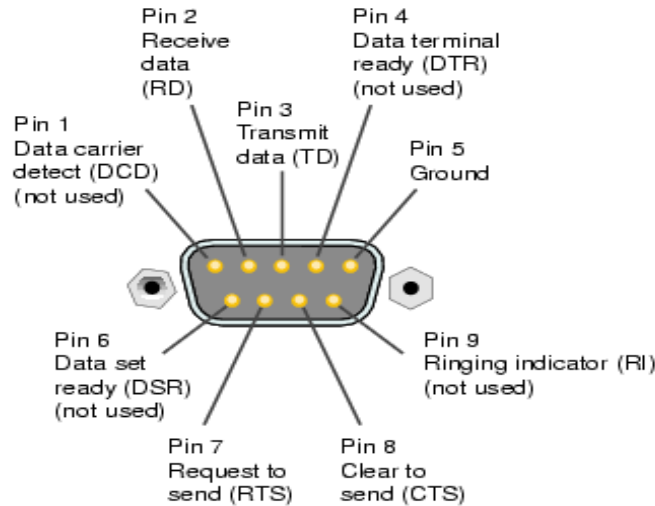


Figure 27: Pin diagram for serial connector [19].

2's compliment in binary. In binary, 2's compliment is a way of expressing signed numbers. If you are not familiar, to convert to a negative number, you take the positive number, change the zeros to ones, and the ones to zeros, then add 1. It is essential for the reader, or computer, to know you are looking at numbers in 2's compliment otherwise the number looks totally different and the same if true for framing the data package. Data chunks can be sent in packets of 5 or 9 bits, the serial we use is 8 bits represented as ASCII characters. Synchronization bits frame the packet and tell the device where a packet begins and ends, while the parity bit is to check for errors. All the bits in a packet should add to an even or odd number (being parity 0 or 1, respectively) and the device can check whether it has correctly observed the start and end of a data packet. For some sophisticated devices there is also flow control that to ensure that the device is not receiving data faster that it can process. This requires continuous feedback between devices and I will not go into detail as the power supplies were not designed with this feature. After understanding all of the basics of serial commands, the next step is to program this in order to automate a sweep of the supplies in place of typing commands into a terminal emulator.

8.3 Serial Commands Using C++

Sending commands to devices over serial and USB are a standard practice and many coding languages have built in function to assist in writing code to do such things. Various languages such as Matlab, Python, C, and C++ all have the capability to open ports, send serial commands, open and write to files and other functions that would be required. Previous co-op students Claire Preston and Liam Lawrence have written code that operates the DC trap and camera equipment in C++ which made it the natural language to choose for this purpose. I will discuss the basics of how to code this type of program before moving on to the final section of the to discuss some of the scope of existing hardware in the TRINAT lab and how to access, modify and add to the code, such as I have done with the power supply code. The basics of accessing and writing to serial ports are as follows.

1. After checking the name of the port that the device is connected to and initializing the required variables in the code, open the ports.
2. Create the termios structure (struct termios settings), which allows for specifying the baud rate, parity, flow control, canonical or non-canonical modes, etc. for the ports and applying these setting to all open ports.
3. Writing a given string, in test cases I hard coded this string, to the port.
4. Closing the port and terminating the code.

Once these basics are accomplished the coder can attempt more sophisticated commands such as an iterating loop where the string command relies in the index of the loop, locking the ports for the duration of the code to prevent accidental cross communication between devices, and more. Using the exact same steps, I was also able to write code that would read a string back from the port (after setting a proper wait timeout between characters) and used the FTDI chip to test that this works, although I did get it to work as mentioned previously the intermittent responses of the supplies caused us to abandon attempts to read information back from the supplies. All code attempts and iterations, as well as finished code is documented, both in notes on the code and additional note files in the folder Documents/Ben Sheldon/Power Supply Remote Control on the HP notebook. With working code, I will now move on to the final section detailing hardware and software in the TRINAT lab and the integration of my code.

9 Running the DC Trap on Stable Species

There are multiple computers used in running the DC atom trap for stable species. There are the **Raspberry Pi 2** and **Raspberry Pi B+**, **trinatlt2**, and **trinatlt3**. The Pi Model 2 runs the main code that uses the General Purpose Input Output (GPIO) pins to control the DAC signals and send commands to the Labjack board. This code was mainly written by Claire Preston, a previous co-op student who upgraded the Pi kernel for running real-time Linux as well as accessing the Flea 3 (a camera model from Point Grey). Code for multiple processes such as accessing the GPIO pins which use the `bcm2835` library, turning on the push-beam (ferries atoms from the first trap to the main chamber), cooling, etc. are all found on the Pi 2. Her impressive report [17] documents these and includes a GPIO pin and DAC diagram reference. Liam has also written code which modifies Claire's work in order to capture images of the trapped cloud to measure the trap lifetime, cloud distribution, and other processes.

To connect to the Pi, simply use the command `ssh -X pi@trinatrpi2` from the computer you are using (most likely the blue HP notebook or `trinatlt3`). The `bcm2835-1.5` folder is a C library for functions that access the GPIO pin board. `wiringPi`, `InitialRTTests_cp`, and other subfolders contain iterations of code for different sequences of the main trap code. The `tenma` folder has code, both C and C++ versions (there were minor syntax changes required), I have written for automating the sweep of the Tenma DC power supplies. This code is documented both with notes within the code itself and a notes file in the folder. To modify if required, simply make a copy of the code you wish to change (`cp filename newfilename`), make the desired changes, use the command `gcc -o filename filename.c` (or `g++` and `.cpp` in C++ correspondingly) to compile the program, and execute with the command `./filename`. The same follows for the Pi B+, with the username `trinatrpi1`. Another useful command, `scp -p filename pi@trinatrpi2:/route/to/desired/folder`, allows for copying files from the host computer to the Pi. The Pi B+ was originally going to be used to run the power supplies as there were access conflicts when attempting to access both the USB ports and Labjack board after integrating my power supply control with existing code. I have since found a way around this and the Pi B+ simply has a folder `tenma` where I initially tested some iterations of my code. The Pi B+ is also running the basic default Pi software and has default features including Mathematica, Wolfram, Python, as well as `gcc` and `g++` compilers.

The main DC trap sequence on the Pi 2 is run from code in the folder `RunTrapSequence_cp`. To modify any code, again make a copy and the necessary modifications or additions first. Go to the makefile (command `emacs Makefile`), and comment out (`#`) the previous executable (EXEC) and replace with the name of your desired program (EXEC = filename) and type the command `make` into the command line of the terminal to compile. As you can see by accessing the makefile, it also uses the code `testseq_functions2_RAC.cpp` to compile, and if you wish to add functions you have defined, you must modify this portion as well. After using the `make` command, your code is ready to be executed, assuming it compiles of course, and the last step is to modify the shell script that calls it into action. `StartSequenceRAC.sh` is the shell script you will want to modify. Again, simply comment out the previous code running, and add your own line (`sudo ./filename`). For running processes that require GPIO pin access and the Labjack board, superuser privileges are required. The power supply code, and accessing the USB ports, does not require superuser privilege and it is good practice to only use the `sudo` command when it is actually required. The shell script also calls `trinatlt2`, the computer running the Flea camera, to start and await triggers in the code to take pictures of the cloud. I was able to get my power supply sweeping code to run in parallel by having the

shell script call both the main sequence code and my power supply code. In order for the supplies to sweep correctly, I modified the existing `TrapSeq_cp3_RAC_lifetimes_ABDAC1toBDC_DC_only` to the file `TrapSeq_cp3_RAC_lifetimes_ABDAC1toBDC_DC_only_sweepTenma2` which writes the loop index n to a file (erasing the previous data in the file) called `n_for_supplies.txt`. The final iteration of C++ code, `power_sweep_cpp_test`, follows the same general steps as outlined in the previous section, but opens the file containing the index n and concatenates this to a string (essentially “ISET1:”+“int(n)”) and sweeps the supplies from 0 to 5A while the loop is iterating in the main sequence. After finishing on the Pi it is important to shutdown properly using the command `sudo shutdown -h now` to prevent corruption of their SD cards.

9.1 Stable Species Preliminary Trap Analysis

There were some issues in the last week of my co-op with running and obtaining photos from the Flea camera that was previously utilized by Claire and Liam. After fixing the camera circuit (and debugging minor issues in the code about when the camera is set to strobe, all iterations are documented in the `log_ben.txt` file but for reference I used `TrapSeq_cp3_RAC_lifetimes_ABDAC1toBDC_DC_only_sweepTenma3.cpp`) and I was able to gather preliminary data for trapping stable species in the DC trap. The shell script previously mentioned calls the power supply and main sequence code which sends a logic signal to the camera telling it to take an image. On the laptop used to run the camera and physica scripts, `trinatl2`, there is a file in the folder `/home/trinat/flycapture/flycapcode/src/cpAsyncTriggerEx` (use the macro `$fly` as a shortcut to this folder) used to set camera settings such as strobe time, exposure time, and various other parameters. The file is called `params.txt` and can be modified before a run if needed. This folder is also where the pictures from a run are stored. Also note, these pictures are deleted once a the next run has begun and the following instructions are how to extract the images for analysis as set up by Liam and Claire. First, enter the command `mvdata` in the command to move all pictures to another folder called `/data`. On the HP notebook use the command `yankdata [foldername]` in order to create a new folder which will copy the data from `trinatl2` and the files are now ready to analyze. In my folder, `/Ben Sheldon/sweepPictures analyzeCloud/` I copied and modified the original code from Liam (which can be found in his physica code folder) used to analyze the cloud pictures.

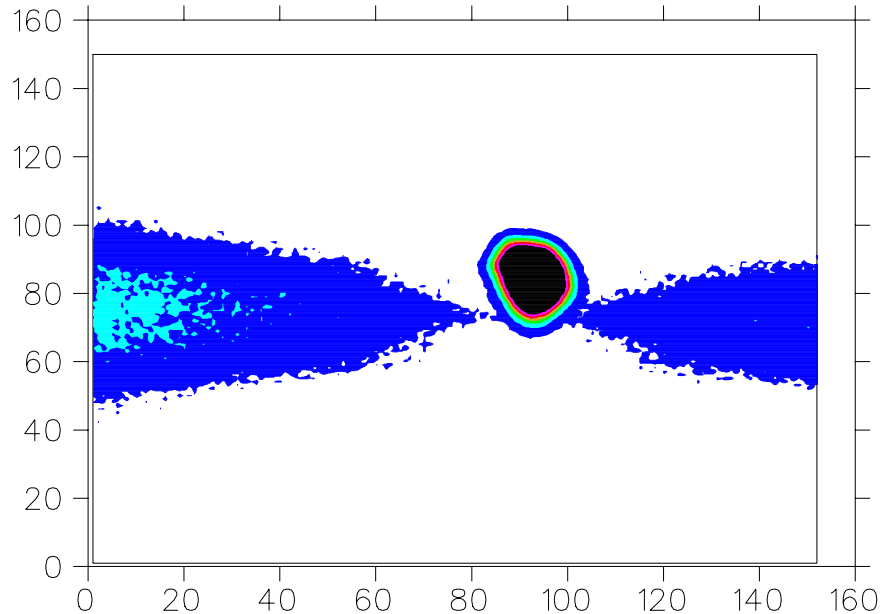


Figure 28: Initial look at the trapped atom cloud using a CCD Flea camera after background has been removed.

In essence, the scripts take x and y projections of the relative intensity of the cloud after subtracting off the background, fit Gaussian functions to each projection (an image is taken during each incrementation of the n loop parameter in the main sequence code) and returns vectors containing the centroid location and width of the cloud in a file called **gaussian.out**. Although the Gaussian shape simply seems intuitive for the cloud you may consult Liam's report for a fairly rigorous proof of why the cloud takes on this form.

I have modified Liam's code to allow me to analyze the x and y projections of the relative cloud intensity for a moving cloud (the above plot shows the dimensions in terms of pixels in the CCD camera and the code for actual Gaussian fits of the cloud have the corresponding conversion factors required). My code for analyzing the cloud shape may be found in the folder **/Documents/Ben Sheldon/sweepPictures/analyzeCloud**. They are similar to Liam's and require inputs of the number of cycles and n iterations per cycle (the `Max_n` parameter defined in the `params.txt` file on the Pi2) and further instruction may be found in comments in the code itself. Below I display the preliminary data I obtained for the rough full sweep of 0 to 5A for current in existing coils on the chamber. Future plans would be to analyze the horizontal position of the cloud accurately over a small current range (say 0.5A) after calibrating the position the camera observes with the actual location of the atom cloud with respect to the trap and chamber. This would allow for precise optimization of the cloud position for a given value of current in the supplies, and hence, a given corresponding magnetic field applied to the atoms. The preliminary data for the sweep of the power supplies shows promising ability to optimize the cloud position and several other important points. An important fact to realize is that the fits of the Gaussian projections are unweighted (there could be some uncertainty applied based on pixel resolution and the number of photons seen per pixel, but would require more time to analyze than I have left in my co-op here) and when physica reports the uncertainties on the center location and width of the Gaussian it defines the errors,

$$\chi^2 = \sum_n \frac{(y_n - f(x_n))^2}{\sigma^2}, \quad (39)$$

(where σ is the error) to be such that χ^2 is equal to 1. This prevents me from using χ^2 as a way to check the goodness of fit and therefore I recommend carefully observing the fit for each image if this code is used. If I were using these fits for an extended analysis I would attempt a more rigorous approach to quantifying the errors in order to get a meaningful χ^2 to judge my fits.

In any case, the analysis yields several important points. First, for a deliberate sweep in the \hat{x} direction, where the cloud is seen to move over a range of $1.5mm$, during a cycle where the current is swept through a range of about 4A (I had to throw away the last two fits as they did not converge and again, I would attempt a much more rigorous fitting process to prevent this if time allowed), the vertical position also changes but only by about $0.25mm$. While running the trap atoms are fed into the main chamber via a push beam at a rate I can call $P(n)$. Atoms in the trap collide with each other and other particles in the non-deal vacuum and I can write the rate at which atoms are lost as $L(n)$. The overall number of atoms in the trap is the difference between these two rates multiplied by a given time duration which can be rewritten as,

$$\frac{dN}{dt} = P - L, \quad (40)$$

and it is clear that the number of atoms in the trap will be constant when $P = L$. For the first cycle (the first 8 points), as the width of the cloud is still increasing, $P > L$, the number of atoms in the trap is exponentially increasing (assuming linear rates). And for completeness, if the push beam is turn off then the number of atoms in the trap will exponentially decay with a given decay constant (similar to the mathematical description of the decay of the magnetic field measured earlier) which is referred to as the lifetime of the trap. During a sweep of the power supplies (before the end of the cycle when the push beam activates to add additional atoms) it is clear that the atom cloud does change size, but by small amounts compared to its average size and the change in cloud shape is directly related to how far the cloud is moved. The horizontal width of the cloud changes by roughly $0.06mm$, with an average width of $0.82mm$, whereas the vertical width changes by roughly $0.01mm$ and has an average width of $1.35mm$. This relative difference in the change in cloud shape between horizontal and vertical components corresponds to the same relative shift in the center of the cloud position for the same horizontal and vertical components. It should be relatively straightforward to add a linear fit through the centroid versus picture plot, as well as to calibrate the axis for the specific current at each picture once that is determined, to optimize the centroid position.

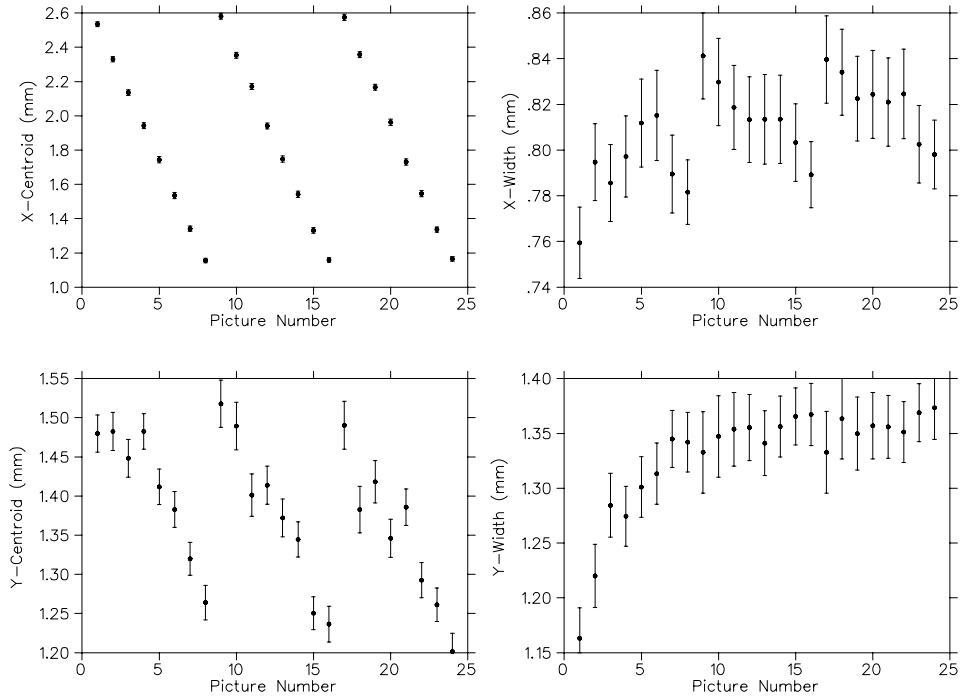


Figure 29: Initial look at the centroid position for x and y projections of the atom cloud during a horizontal sweep.

Unfortunately, this was as far as I was able to get on the analysis of the atom cloud before my co-op ended. The next steps as outlined previously would be to perform a more rigorous analysis of the position of the cloud over a much smaller current range in order to optimize the trap position. The same procedure could be done for the vertical coils I have been studying to determine the optimum current in them as well and how a magnetic field changing in time effects the cloud shape. Further work would be to begin testing the full AC trap (the RAC-MOT) which involves turning on and off the trap to allow for polarization. A quantitative study of the fluorescence of the atoms, which is related to the polarization, could be done to study how the additional magnetic fields effect polarization which is crucial for full experiments with the unstable species observed to study beta decay.

10 Acknowledgements

I would just like to say thank you to everyone I worked with in the TRINAT group for their time; John, Alexandre, Melissa, and James, as well as to the number of speakers who presented during the undergraduate seminar series during the last couple of months.

11 References

- [1] P.D. Shidling, D. Melconian, et al., *Precision half-life measurement of the β^+ decay of ^{37}K* (Physical Review C)
- [2] D.J. Griffiths, *Intro to Electrodynamics*, 4th ed. (Pearson, 2012)
- [3] WaveMetrics, IGOR PRO software (<https://www.wavemetrics.com/>)
- [4] URI, *Physics 204*, University of Rhode Island Course Notes (<http://www.phys.uri.edu/gerhard/PHY204/tsl215.pdf>)

- [5] Hyun Youk, *Numerical study of quadrupole magnetic traps for neutral atoms: anti-Helmholtz coils and a U-chip*, Canadian Undergraduate Physics Journal
- [6] Image obtained from <http://www.mecamagnetic.com/theory-principle.php>
- [7] E.R. Javor, T. Anderson, *Design of a Helmholtz Coil For Low Frequency Magnetic Field Susceptibility Testing*, Naval Undersea Warfare Center, Newport (<https://www.ipen.br/biblioteca/cd/ieee/1999/Proceed/00132.pdf>)
- [8] Online calculator for the inductance of copper wires (<https://ampbooks.com/home/amplifier-calculators/wire-inductance/>)
- [9] P. Horowitz, W. Hill, *The Art of Electronics* (Cambridge University Press)
- [10] I. Vollrath, *Magnetic Field Turn-Off Investigation* (Triumpf Report)
- [11] L. Lawrence, *2016 Triumpf Summer Co-op Report* (Triumpf Report)
- [12] B. Fenker, *Precise Measurement of the β -Asymmetry in the Decay of Magneto-Optically Trapped, Spin-Polarized ^{37}K* (Texas A&M University, PhD Thesis)
- [13] Magnetic Shield Corporation (<http://www.magnetic-shield.com/pdf/cp-1-brochure-web-spread.pdf>)
- [14] E. Butkov, *Mathematical Physics* (Addison-Wesley 1968)
- [15] A. Smith, R. Kessel, et al., *Modulation Effects in Wedge and Strip Anodes* (Review of Scientific Instruments 60)
- [16] Tenma Remote Control Commands (<https://www.element14.com/community/docs/DOC-75108/1/protocol-information-for-tenma-72-2550-and-tenma-72-2535-qa-window-driver>)
- [17] C. Preston, *Upgrading TRINAT Control System and Optimizing Temperature* (Triumpf Report)
- [18] Image obtained from <https://en.wikipedia.org/wiki/Photomultiplier#/media/File:PhotoMultiplierTubeAndScintillator>
- [19] Image obtained from <http://codesamplez.com/programming/serial-port-communication-c-sharp>
- [20] Specs for the PMT model 9823B <https://my.et-enterprises.com/pdf/9823B.pdf>

12 Appendices

12.1 Appendix 1: Physical Concepts

- **Beta Decay** - occurs in nuclei which are unstable due to the number of protons and neutrons. Beta minus (β^-) decay is when a neutron decays into a proton, an electron (in order to conserve the initial 0 charge), and an antineutrino as described by, $n \rightarrow p + e^- + \bar{\nu}$. On the other hand, Beta plus (β^+) decay is when a proton decays into a neutron, a positron (anti electron, again to conserve charge), and a neutrino as described by, $p \rightarrow n + e^+ + \nu$. The atoms in which each type of beta decay occurs depend where in they sit with respect to the valley of stability in the chart of nuclides. The chart of nuclides is a scatter plot of proton (Z number) versus neutron (N) of all known nuclides. The center line of this plot is known as the valley of stability as nuclides near the edge have much shorter lifetimes than those near the center.
- **Spin** - in order to understand spin polarization, it is important to understand the concept of spin, where I will use the classical analogy. To describe a planets total angular momentum, one must take into account the orbital component (the Earth orbiting about the center of mass of the Earth-Sun system) and the rotational angular momentum (Earth rotating on its axis). You could imagine a giant arrow through the Earth depicting the rotational axis. For quantum mechanical particles there is no classical analogue (quantum particles do not rotate about an axis), but the planetary rotation model can help to understand it. For quantum mechanical particles, a component of angular momentum

comes from the phenomena spin which is quantized. For example, an electron is a Fermion (which have half integer spins) and has a spin of $1/2$, and can either be in the $+1/2$ or $-1/2$ state. If particles are in the same spin state, they are said to be aligned, and this is where thinking of aligning planetary rotational axis can be helpful, and if they are in the opposite state, they are anti-aligned. With a large ensemble of particles, the measure of spin polarization is the degree to which all the particles have their spin aligned along a certain given axis.

- **Doppler cooling** - is the method used to slow and ($T \propto E_k$), hence, cool atoms. Shining a laser detuned slightly below a transition level in an atom toward it means that if the atoms are moving toward the laser, the apparent frequency of the laser will increase due to the Doppler effect. You can think of someone dropping a rock into water. If you are stationary, the wave will hit you with a frequency f_0 . If you now move toward the source of those waves, more will hit you the faster you move and the frequency with which you observe wave hits will be $f > f_0$. The same is true for the atoms moving away from the laser in that the frequency will be lower and hence less even less likely to absorb a photon since the laser is already detuned below the transition frequency. When moving toward the laser, and absorbing more photons, the atoms will slow down due to conservation of the momentum imparted by the photon (which is opposite the original motion of the atom). The process of absorption happens along a specific direction. Now that the atom has absorbed a photon, and an electron has risen to an excited state, it will want to decay and emit the photon, and there is no preference on the direction of emission of the photon, and so the momentum change is in a random direction. The overall effect is that the atom is slowed along an axis specified by the laser direction. Using lasers oriented along the x , y and z axis, slowing and effective cooling of the atoms occurs in all three dimensions.
- **Weak Interaction** - is the force responsible for radioactive decay. In particle physics, forces are mediated by force carriers and the range of the force is inversely proportional to the mass of the force carrier. For example, using particle physics theory to explain the electromagnetic interaction, photons are the force carrier and hence have infinite range due to the photon having zero mass, although from classical electromagnetism we know that the force falls as $1/r^2$ and although has infinite range, has diminishing influence at larger distances. The weak interaction is mediated by the W^+ , W^- and Z bosons which are more massive than the proton and neutron. The consequence of which is that the weak force is said to be a short range force. The weak interaction occurs between fundamental particles, quarks, and it is the result of the change of the flavor of quarks that causes a proton to turn into a neutron and vice versa and the force carrier, the boson, quickly decay into the secondary products, the beta particle and neutrino.
- **Neutrino Detection** - is not done directly in the TRINAT lab due to the fact that neutrinos are chargeless and extremely light. Charged particles are easy to detect due to the ability to use manipulate their trajectory with electric and magnetic fields and due to the fact that they interact via the Coulomb force with electrons in material.
- **Quadrupole Field** - describes the characteristics of the magnetic field created when current is flowing in opposite directions in two coils. The field along the coil axis changes sign at the center point between coils (and linearly in the region near the center) such that for atoms at the center, a Zeeman shift to the energy levels of the electron orbitals is induced when the atom moves away from $z = 0$. The magnitude of the Zeeman shift can be calculated using perturbation theory where the magnetic field is the perturbation to the potential in the Hamiltonian describing the atom. This brings the atoms closer to the frequency of the laser light and works in parallel with the idea of Doppler cooling.